

Star-forming regions of the Aquila rift cloud complex

II. Turbulence in molecular cores probed by NH₃ emission[★]

S. A. Levshakov^{1,2,3}, C. Henkel^{4,5}, D. Reimers¹, and M. Wang⁶

¹ Hamburger Sternwarte, Universität Hamburg, Gojenbergsweg 112, 21029 Hamburg, Germany
e-mail: lev@astro.ioffe.rssi.ru

² Ioffe Physical-Technical Institute, Polytekhnicheskaya Str. 26, 194021 St. Petersburg, Russia

³ St. Petersburg Electrotechnical University “LETI”, Prof. Popov Str. 5, 197376 St. Petersburg, Russia

⁴ Max-Planck-Institut für Radioastronomie, Auf dem Hügel 69, 53121 Bonn, Germany

⁵ Astronomy Department, King Abdulaziz University, PO Box 80203, 21589 Jeddah, Saudi Arabia

⁶ Purple Mountain Observatory, Key Laboratory of Radio Astronomy, Chinese Academy of Sciences, 210008 Nanjing, PR China

Received 28 February 2014 / Accepted 16 May 2014

ABSTRACT

Aims. We intend to derive statistical properties of stochastic gas motion inside the dense, low-mass star-forming molecular cores that are traced by NH₃(1, 1) and (2, 2) emission lines.

Methods. We use the spatial two-point autocorrelation (ACF) and structure functions calculated from maps of the radial velocity fields.

Results. The observed ammonia cores are characterized by complex intrinsic motions of stochastic nature. The measured kinetic temperature ranges between 8.8 K and 15.1 K. From NH₃ excitation temperatures of 3.5–7.3 K, we determine H₂ densities with typical values of $n_{\text{H}_2} \sim (1-6) \times 10^4 \text{ cm}^{-3}$. The ammonia abundance, $X = [\text{NH}_3]/[\text{H}_2]$, varies from 2×10^{-8} to 1.5×10^{-7} . We find oscillating ACFs, which eventually decay to zero with increasing lags on scales of $0.04 \lesssim \ell \lesssim 0.5 \text{ pc}$. The current paradigm supposes that the star-formation process is controlled by the interplay between gravitation and turbulence with the latter preventing molecular cores from a rapid collapse due to their own gravity. Thus, oscillating ACFs may indicate a damping of the developed turbulent flows surrounding the dense but less turbulent core, a transition to dominating gravitational forces and, hence, to gravitational collapse.

Key words. ISM: molecules – ISM: kinematics and dynamics – radio lines: ISM – line: profiles – techniques: spectroscopic – ISM: clouds

1. Introduction

In the present study, we continue our survey (Levshakov et al. 2013a, hereafter Paper I) of dense cores in Aquila in the NH₃(1, 1) and (2, 2) lines. The targets selected are based on an extended CO survey with the Delingha 14-m telescope (Zuo et al. 2004), the CO data of Kawamura et al. (1999, 2001), and the optical data of Dobashi et al. (2005), which is limited in the latter case by areas with $A_V > 6 \text{ mag}$. More than 150 sources were detected in CO and ¹³CO at $\lambda \sim 3 \text{ mm}$ with the Delingha telescope (Wang, priv. comm.). The angular resolution in these observations was about 50'' (full width at half power, FWHP), which is quite close to that of Effelsberg at *K*-band ($\text{FWHP} \approx 40''$). Subsequently, the NH₃ (1, 1) and (2, 2) emission lines were observed at Effelsberg with high spectral resolutions. Channel widths were $\Delta_{\text{ch}} = 0.015, 0.038, \text{ and } 0.077 \text{ km s}^{-1}$ (Paper I; Levshakov et al. 2013b). Here, we report on observations of newly discovered three cores located in the Serpens South star-forming region, and one core from the Cepheus Flare giant molecular cloud for comparison.

The current work is mainly focused on investigating the statistical characteristics of the spatial velocity field. The most accurate information on the velocity field is provided by two-dimensional maps of molecular lines toward a specific cloud

with velocity providing a third dimension. It follows that the observed profile of an optically thin spectral line is a line of sight integral of emitted photons and that the measured line center, linewidth, and other parameters result from a complex combination of such stochastic fields as gas density, velocity, temperature, and relative abundance. To obtain the spatial distributions of physical parameters and kinematic characteristics of the velocity field with the highest possible sensitivity, bright ammonia sources have been mapped.

Among the most sensitive species that trace the innermost parts of low-mass dense cores, the ammonia molecule NH₃ plays a particular role:

- The observed inversion transitions NH₃(*J*, *K*) = (1, 1) and (2, 2) at 23.7 GHz contain optically thin ($\tau \lesssim 1$) and narrow ($\text{FWHP} \equiv \Delta v \lesssim 1 \text{ km s}^{-1}$) spectral features¹.
- In contrast to the carbon-chain molecules which represent an “early” chemical state because of later freeze-out onto dust grains and gas phase reactions, ammonia represents a “more evolved” chemical stage of evolution and is typically observed in regions where the density approaches 10^5 cm^{-3} (Gwenlan et al. 2000; Tafalla et al. 2004).
- The rotational transitions with $\Delta K \neq 0$ are forbidden for ammonia; that is, relative populations of ammonia rotational levels depend only on collisions and thus measure the gas

[★] Appendix A is available in electronic form at <http://www.aanda.org>

¹ Here *J* is the total angular momentum, and *K* is the component of *J* parallel to the molecular main axis.

Table 1. Peak intensities of NH₃(1, 1) line emission toward SS1, SS2, and L1251C.

Source	Peak Id. ^a	Position		Offset $\Delta\alpha, \Delta\delta$ ($''$, ($''$))	T_{MB}^b (K)	V_{LSR}^c (km s ⁻¹)	Δv^c (km s ⁻¹)	Date (d-m-y)
		α_{2000} (h: m: s)	δ_{2000} ($^{\circ}$: $'$: $''$)					
SS1		18:29:09.6	-02:05:40	0, 0	0.9(1)	6.41(1)	0.69(2)	16-03-13
	α			-40, 0	1.1(1)	6.139(6)	0.54(1)	16-03-13
				-40, -40	0.8(1)	6.32(2)	0.95(5)	16-03-13
SS2A	η	18:29:05.1	-01:42:00	0, 0	0.8(1)	7.05(1)	1.04(3)	18-03-13, 09-05-13
	α			-40, 200	2.9(3)	7.361(6)	0.47(1)	22-03-13
	β			-80, -40	2.4(2)	6.622(3)	0.416(6)	18-03-13, 22-03-13
	γ			-360, 320	2.0(2)	6.457(4)	0.24(1)	23-03-13
	δ			-240, 240	1.9(2)	6.781(6)	0.30(1)	23-03-13
	ε			-240, 440	1.4(1)	7.175(7)	0.22(2)	23-03-13
	ζ			120, 120	1.1(1)	7.526(9)	0.24(2)	23-03-13
	θ			-80, -160	0.8(1)	8.24(3)	0.46(2)	23-03-13
SS2B	α	18:29:47.8	-01:37:20	0, 0	2.3(2)	8.187(2)	0.259(5)	24-03-13, 09-05-13
	β			40, 40	2.3(2)	8.322(2)	0.287(4)	24-03-13, 09-05-13
	γ			240, 80	2.2(2)	8.178(3)	0.426(6)	09-05-13
	δ			120, 0	1.7(2)	8.048(3)	0.26(1)	08-05-13
	ε			-20, 100	1.6(2)	8.14(1)	0.28(2)	24-03-13
SS2C	α	18:31:09.2	-01:34:40	0, 0	0.4(1)	8.49(3)	0.25(3)	09-05-13
L1251C	α	22:35:53.6	+75:18:55	0, 0	3.9(2)	-4.722(3)	0.290(7)	23/24-03-13, 09-05-13

Notes. ^(a) Greek letters mark peaks of ammonia emission indicated in Figs. 2–6. ^(b) The numbers in parentheses correspond to a 1σ statistical error on the last digit. ^(c) Linewidth (FWHP).

kinetic temperature T_{kin} , which is not affected by the presence of turbulent velocity components (Juvela et al. 2012).

- The inversion transitions have, in turn, magnetic hyperfine structure (hfs) components of different intensities, which provide a convenient tool to estimate the line optical depth τ_{JK} , the excitation temperature T_{ex} , and the column densities N_{JK} (Ungerechts et al. 1980; Paper I).
- Detailed balance calculations between collisions and radiative processes also provide a relation between n_{H_2} , T_{kin} , and T_{ex} (Ho & Townes 1983).
- The comparison of the observable linewidths of the hfs components with their thermal widths can be used to estimate the contribution of non-thermal (turbulent) velocity motion to the line broadening (Fuller & Myers 1993).

Molecular cores, which are dense regions ($n_{\text{H}_2} \sim 10^4 \text{ cm}^{-3}$) of low kinetic temperature ($T_{\text{kin}} \sim 10 \text{ K}$), small linear sizes ($L \sim 0.1 \text{ pc}$) and masses ($M \sim M_{\odot}$) embedded in molecular clouds ($n_{\text{H}_2} \sim 10^2 \text{ cm}^{-3}$, $T_{\text{kin}} \sim 30 \text{ K}$, $L \sim 10 \text{ pc}$, $M \sim 10^2 M_{\odot}$), are believed to be the direct progenitors of individual low mass stars, binary systems, small stellar groups, or clusters. Their physical properties are the key issue for gravitational fragmentation studies, since low temperatures and relatively high gas densities favor gravitational contraction and collapse. Observations and numerical simulations show that the origin of molecular clouds is due to the interplay of gravity and turbulence. Turbulence is an effective mechanism creating overdensities in molecular clouds to initiate gravitational contraction and to control star-formation rates in interstellar clouds. With rotation, magnetic fields, and ambipolar diffusion, turbulence prevents molecular clouds from a rapid collapse due to their own gravity.

Turbulent (stochastic) motions in the cold interstellar medium (ISM) are observed to be supersonic and are characterized by various physical processes that are linked nonlinearly over a wide range of scales from $\sim 150 \text{ pc}$ (the energy injection scale from supershells, e.g., Miesch & Bally 1994) down to the Kolmogorov dissipation scale of $\sim 10^{14} \text{ cm}$, which is the

smallest turbulent scale below which viscous dissipation becomes dominant (e.g., Kritsuk et al. 2011). However, in spite of numerous theoretical and observational works (see the reviews of Elmegreen & Scalo 2004; McKee & Ostriker 2007; Maudy 2011; Klessen 2011; Crutcher 2012; Kennicutt & Evans 2012; Hennebelle & Falgarone 2012; Myers 2014), real parameters of the small-scale stochastic motion in dense cores are still poorly known. This makes the detailed study of molecular cores in ammonia lines particularly important.

The content of the paper is the following. Observations are described in Sect. 2. Section 3 deals with physical parameters of the observed dense cores. In Sect. 4, the velocity structure of the cores is analyzed by means of the autocorrelation and structure functions of the components of the velocity field parallel to the line of sight. The results obtained are summarized in Sect. 5. Appendix A outlines the computational procedure used to analyze ammonia spectra. The observed NH₃ spectra are presented in this appendix as well.

2. Observations

The ammonia observations were carried out with the Effelsberg 100-m telescope² in two observing sessions between March 16–24, 2013, and in one session on May 8–9, 2013 (Table 1). The measurements were performed in the frequency switching and position switching modes with the backend eXtended bandwidth FFTS (XFFTS) operating at 100 MHz bandwidth and providing 32 768 channels for each polarization. The resulting channel width was $\Delta_{\text{ch}} = 0.039 \text{ km s}^{-1}$, but the true velocity resolution is 1.16 times coarser (Klein et al. 2012). The NH₃ lines were measured with a K-band high-electron mobility transistor (HEMT) dual channel receiver, yielding spectra with a spatial resolution of $40''$ (FWHP) in two orthogonally oriented linear polarizations at the rest frequency of the $(J, K) = (1, 1)$

² The 100-m telescope at Effelsberg, Germany, is operated by the Max-Planck-Institut für Radioastronomie on behalf of the Max-Planck-Gesellschaft (MPG).

(23 694.495487 MHz) and (2, 2) (23 722.633644 MHz) lines (Kukolich 1967). Averaging the emission from both channels, the typical system temperature (receiver noise and atmosphere) is 100 K on a main beam brightness temperature scale.

The pointing was checked every hour by continuum cross scans of nearby continuum sources. The pointing accuracy was better than 5". The spectral line data were calibrated by means of continuum sources with a known flux density. We mainly used G29.96–0.02 (Churchwell et al. 1990). With this calibration source, a main beam brightness temperature scale, T_{MB} , could be established. Since the main beam size (40") is smaller than most core radii (>50") of our sources, the ammonia emission couples well to the main beam and, thus, the T_{MB} scale is appropriate. Compensations for differences in elevation between the calibrator and the source were $\lesssim 20\%$ and have not been taken into account. Similar uncertainties of the main beam brightness temperature were found from a comparison of spectra toward the same position taken at different dates.

3. Physical properties of molecular cores

Below, we describe observations of the Cepheus molecular core L1251C, and the two sources SS1 and SS2 (the latter consists of three separate objects labeled A, B, and C) located in the star-forming region Serpens South, which is associated with the Aquila rift. With SS3 analyzed for the first time in ammonia lines in Paper I, these sources form a triangle on the plane of the sky with sides 13'0 (SS1–SS3), 22'3 (SS3–SS2A), and 23'7 (SS2A–SS1). The SS3 lies directly to the north of the central Serpens South protocluster (Gutermuth et al. 2008) and coincides with a HC₇N(21–20) gas concentration at RA = 18^h:29^m:57^s, Dec = –1°:58':55" (J2000) dubbed “1b” in Friesen et al. (2013). The SS3 was recently observed in the HC₅N(9–8) emission line (Levshakov et al. 2013b) and in lines of N₂H⁺, H¹³CO⁺, NH₂D, SiO, HCO⁺, CS, and HCN (Kirk et al. 2013; Tanaka et al. 2013). However, SS1 and SS2 lie outside the regions mapped in these studies: the former in the west and the latter in the northwest direction to the Serpens South protocluster (see Fig. 1 in Friesen et al. 2013).

Figure 1 shows dark cores detected in the Serpens South area in the 2 Micron All Sky Survey Point Source Catalog (2MASS PSC) by Dobashi (2011, hereafter D11). Ammonia cores observed in the present work are marked by arrows. Numbers in parentheses denote dust cores compiled in Dobashi’s catalog. The following selection criteria were applied: a continuous area having $A_V^{\text{core}} \geq 1.5$ mag ($\sim 7.5\sigma$) with a single peak higher than the boundary by ≥ 1 mag ($\sim 5\sigma$) was defined as a candidate for a dark core. The extinction value at the peak position for the Dobashi core #1184 (the counterpart of SS1) is $A_V^{\text{core}} = 9.6$ mag. For the three cores #1205, #1220, and #1227 (the counterparts of SS2 A, B and C), they are 13.5, 10.2, and 4.8 mag, respectively, and it is 15.1 mag for the core #1194 (the counterpart of SS3). We note that the cores #1184, 1220, and 1227 are labeled by the number #279 in the optical photographic database by Dobashi et al. (2005), and the cores #1205 and 1194 by #279P22 and 279P7, respectively. Surprisingly, the objects SS2B and SS2C were not detected in CO lines from the Delingha observations. Both of them were found serendipitously in our ammonia survey (see Sect. 3.2).

3.1. Serpens South 1 (SS1)

Our NH₃ observations cover the whole molecular core SS1 and consist of 30 spectra obtained at the positions marked by crosses

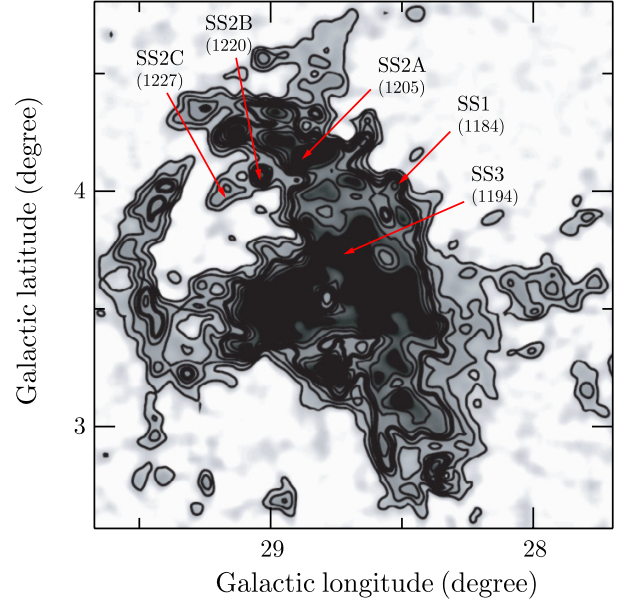


Fig. 1. Dark cores from the 2 Micron All Sky Survey Point Source Catalog (2MASS PSC) by Dobashi (2011). Contours start from $A_V^{\text{core}} = 1.5$ mag; the increment is 1.5 mag, and thick lines are drawn at every four contours. The positions of the ammonia cores observed with the Effelsberg 100-m telescope are marked by arrows (SS3 was analyzed in Paper I). Numbers in parentheses denote individual dust cores compiled in Dobashi’s catalog.

in Fig. 2a. We adopt $D = 203$ pc as the distance to the source (Paper I). The angular size of the major (NE–SW) and minor (SE–NW) axis³ is $175'' \times 125''$. This corresponds to the linear dimensions $a \times b \approx 0.17$ pc \times 0.12 pc and to the mean diameter $L = \sqrt{a \cdot b} \approx 0.14$ pc. Dust emission at $2 \mu\text{m}$ was detected from core #1184 (D11), the counterpart of the source SS1. The dust emission is seen from an area $S = 79.8$ arcmin² (D11), corresponding to an extent of $\sim 536''$, which is about four times the ammonia emitting region. The core is situated slightly above the Galactic plane ($b \approx 4^\circ$ corresponding to ~ 15 pc)⁴ and consists of a dense core labeled α in Fig. 2b and a weak filament pointing southwest. An infrared source IRAS 18265–0205 (Beichman et al. 1988) located at the northeastern edge of the core is marked by a red star in Fig. 2. It is not clear if this IR source is physically connected with the molecular core since no related perturbations or systematic flows are seen in Fig. 2b.

The extended central region of SS1 covers three adjacent positions of similar brightness temperature $T_{\text{MB}} \sim 1$ K (see Table 1), which are not resolved at our angular resolution of 40" (the corresponding spatial resolution is ~ 0.04 pc). However, the positions show essentially different radial velocities, $V_{\text{LSR}} = 6.41$, 6.139, and 6.32 km s^{–1}, and linewidths, $\Delta v = 0.69$, 0.54, and 0.95 km s^{–1}, that may point to the existence of substructure at scales < 0.04 pc. Formally, the position (–40", 0") with the narrowest line and a slightly higher line temperature is referred to as the “ α peak”.

The model fit to the observed NH₃(1, 1) and (2, 2) spectra is shown in Fig. A.1, and the corresponding model parameters are given in Table A.1. Toward the (0", 0") position, we measured a kinetic temperature of $T_{\text{kin}} \sim 15$ K, which is rather high for

³ The core size is defined at the half-maximum (50%) contour of the integrated intensity map of the corresponding emission line.

⁴ This implies that the core is in total ~ 35 pc above the Galactic mid-plane, if the Sun’s distance is ~ 20 pc (Humphreys et al. 1995).

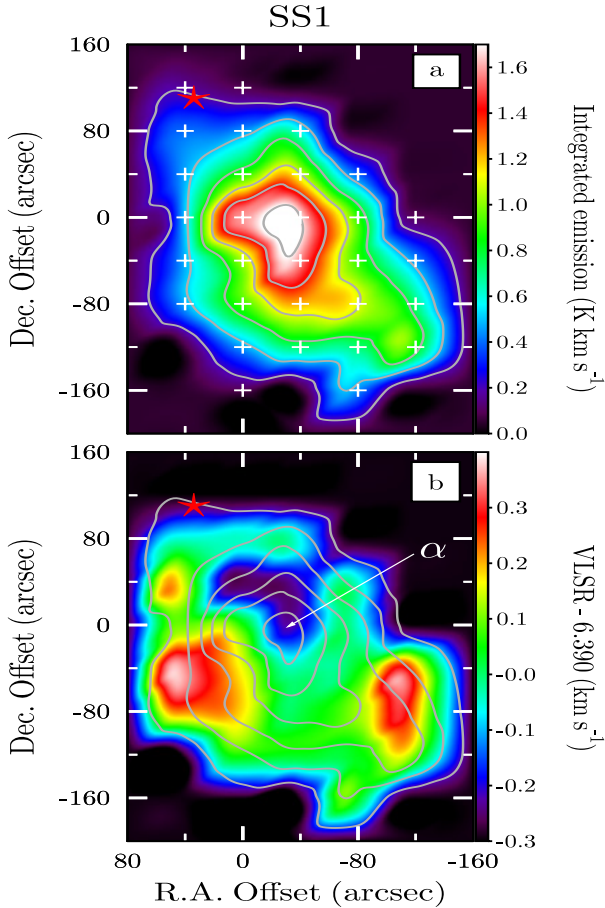


Fig. 2. **a)** $\text{NH}_3(1,1)$ intensity map ($\int T_{\text{MB}} dv$) of the molecular core SS1. The starting point for the contour levels is 0.2 K km s^{-1} ; the increment is 0.3 K km s^{-1} . Crosses mark measured positions; the red star indicates the location of the IR source IRAS 18265–0205 (Beichman et al. 1988). **b)** $\text{NH}_3(1,1)$ radial velocity field (color map) shown after subtracting the mean radial velocity ($\langle V_{\text{LSR}} \rangle = 6.390 \text{ km s}^{-1}$). The NH_3 peak is labeled as in Table 1. The $(0,0)$ map position is RA = 18:29:09.6, Dec = $-02:05:40$ (J2000).

dense molecular cores, and a typical gas density of $n_{\text{H}_2} \sim (2-3) \times 10^4 \text{ cm}^{-3}$.

At the α peak, the total ammonia column density $N_{\text{tot}} = 1.8 \times 10^{14} \text{ cm}^{-2}$ and the gas density $n_{\text{H}_2} = 1.8 \times 10^4 \text{ cm}^{-3}$ (Table A.1) correspond to the ammonia abundance ratio $X = [\text{NH}_3]/[\text{H}_2] = 2 \times 10^{-8}$, which is in line with other sources (e.g., Dunham et al. 2011).

The measured linewidth at the α peak $\Delta v = 0.54 \text{ km s}^{-1}$ and the kinetic temperature $T_{\text{kin}} = 13.6 \text{ K}$ (Table A.1) give a thermal velocity $v_{\text{th}} = 0.11 \text{ km s}^{-1}$ (Eq. (A.6)), and a turbulent velocity dispersion $\sigma_{\text{turb}} = 0.22 \text{ km s}^{-1}$ (Eq. (A.7)). The dispersion of the line-of-sight velocity component of bulk motions is comparable to the sound speed $c_s \approx 0.22 \text{ km s}^{-1}$ (Eq. (A.8)); that is, non-thermal motions are transonic with the Mach number $\mathcal{M}_s = 1 \pm 0.1$ (Eqs. (A.9), (A.10)). However, supersonic motions with local $\mathcal{M}_s = 1.2 \pm 0.1$ and 1.8 ± 0.1 are observed toward the two other peaks at offsets $(0'', 0'')$ and $(-40'', -40'')$, respectively. The transition between transonic and supersonic gas motions is observed over a beam width (0.04 pc). For example, the change in the velocity dispersion, $d\sigma_{\text{turb}}/dr$, between the α peak and the offset $(-40'', -40'')$ is $d\sigma_{\text{turb}}/dr \gtrsim 4 \text{ km s}^{-1} \text{ pc}^{-1}$, which is comparable to the change $d\sigma_{\text{turb}}/dr \approx 3 \text{ km s}^{-1} \text{ pc}^{-1}$ observed toward the B5 region in Perseus (Pineda et al. 2010). Such a

sharp transition – the increase of the velocity dispersion by a factor 1.5–2 in less than 0.04 pc – is also observed in other cores mapped in the $\text{NH}_3(1,1)$ line at high angular resolutions (see, e.g., the review by André et al. 2013).

The gas density, n_{H_2} , determined for the three central condensations and the ammonia linewidths, Δv , (Table A.1) can be used to estimate a core mass. Using the mean gas density $n_{\text{H}_2} = 2.4 \times 10^4 \text{ cm}^{-3}$ and the core radius $R \sim 0.07 \text{ pc}$, and assuming spherical geometry, we find a core mass $M \sim 2 M_{\odot}$ (the mean molecular weight is 2.8). On the other hand, the virial mass (Eq. (A.11)) calculated from the weighted mean linewidth $\Delta v = 0.77 \text{ km s}^{-1}$ and accounting for the dominating non-thermal line broadening is $M_{\text{vir}} \sim 10 M_{\odot}$. The observed difference in the masses could be due to deviations from a uniform gas density distribution and a core ellipticity.

3.2. Serpens South 2 (SS2)

Starting with observations of the main source SS2A in the position switching mode, we detected serendipitously two other ammonia compact cores, which we refer to as SS2B and SS2C (Fig. 3). Their spectral lines are shifted with respect to those of SS2A: $V_{\text{LSR,A}} = 7.4 \text{ km s}^{-1}$, $V_{\text{LSR,B}} = 8.2 \text{ km s}^{-1}$, and $V_{\text{LSR,C}} = 8.5 \text{ km s}^{-1}$ (Table 1). The source SS2B was completely mapped down to its edge, whereas we did not have enough time to investigate the area around SS2C. For this reason, only three $\text{NH}_3(1,1)$ spectra of SS2C can be shown in Fig. A.2.

The strongest ammonia emission measured at $V_{\text{LSR}} = 8.5 \text{ km s}^{-1}$ toward SS2C is one of the narrowest lines ($\Delta v = 0.25 \pm 0.03 \text{ km s}^{-1}$) observed in our survey (see Table 1). If we assume a kinetic temperature $T_{\text{kin}} \sim 10 \text{ K}$ for this source, then the estimated $\sigma_{\text{turb}} \sim 0.08 \text{ km s}^{-1}$ would imply gas moving at subsonic velocities with $\mathcal{M}_s \approx 0.4 \pm 0.2$. The dust core #1227 from Dobashi’s catalog (D11), a counterpart of the source SS2C, occupies a region of 65.8 arcmin^2 with a linear size of about $490''$. This is the only information available for this source at the moment. In the following subsections, we will concentrate on our results obtained for SS2A and SS2B.

3.2.1. SS2A

The source SS2A is an example of a complex molecular core consisting of at least eight ammonia peaks (Fig. 4). Individual NH_3 peaks are labeled α through θ in order of decreasing peak line brightness temperature T_{MB} (Table 1). The ammonia emission is observed from an elongated irregular structure in the NW-SE direction over an area of $\approx 600'' \times 400''$ ($\approx 0.6 \text{ pc} \times 0.4 \text{ pc}$). The associated dust core #1205 extends over an area of 170.6 arcmin^2 (D11) and has a linear size of about $780''$. The core harbors a few IR sources and protostars marked by red crosses and red stars in Fig. 4. The η peak coincides with the class 0 protostar MM2, which is a condensation of several infrared sources (Maury et al. 2011). The measured positions are marked by white crosses.

Figure 4b shows a rather high amplitude of the radial velocity fluctuations, $\delta V_{\text{LSR}} \approx \pm 1 \text{ km s}^{-1}$, as compared with the velocity fields of SS1 (Fig. 2) and SS2B (Fig. 5b), where the observed amplitude is $\delta V_{\text{LSR}} \approx \pm 0.3 \text{ km s}^{-1}$. High velocity perturbations in SS2A resemble a velocity pattern measured toward the core Do279P12, where $\delta V_{\text{LSR}} \approx \pm 1 \text{ km s}^{-1}$ and the $\text{NH}_3(1,1)$ and $(2,2)$ lines are split at some positions into two components (Paper I).

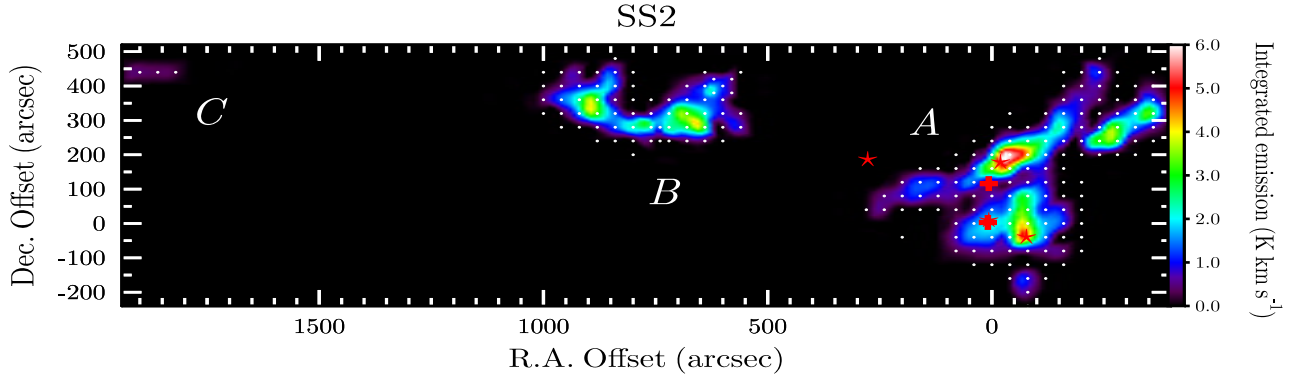


Fig. 3. The integrated NH₃(1, 1) emission ($\int T_{\text{MB}} dv$) of the molecular core SS2 (source A) and two serendipitously detected cores (sources B and C). White dots mark measured positions; crosses indicate the location of the IR sources IRAS 18264–0143 and IRAS 18264–0142 (Beichman et al. 1988), and stars determine Class 0 protostars (Maury et al. 2011). The (0, 0) map position is RA = 18:29:05.1, Dec = –01:42:00 (J2000).

A similar picture of a split but not completely resolved line profile showing a redward asymmetry is observed toward SS2A. The ammonia profiles depicted in Fig. A.3 at offsets (–40′′, 0′′), (–80′′, 0′′), and (–80′′, 40′′) cannot be described by a single component model but require a second component shifted with respect to the first one by 0.8, 0.7, and 0.9 km s^{–1}, respectively (see Table A.1). On the other hand, the ammonia magnetic hfs components are optically thin ($\tau < 1$) at these velocity offsets. Therefore, the observed asymmetries must be due to kinematics rather than radiative transfer effects expected at high optical depths⁵.

The NH₃ linewidths range in a wide interval between $\Delta v = 0.22$ km s^{–1} and 1.04 km s^{–1} (Table 1). Unfortunately, the second inversion line NH₃(2, 2) was not detected at all ammonia peaks listed in Table 1, and we were not able to directly estimate the kinetic temperature and, thus, the contribution of turbulent and thermal motions to the line broadening at all offsets. However, at 15 positions listed in Table A.1, we observed both the (1, 1) and (2, 2) lines and, thus, the values of σ_{turb} and v_{th} can be calculated directly. The maximum dispersions of $\sigma_{\text{turb}} = 0.22$ km s^{–1} ($T_{\text{kin}} = 14.2$ K) and $\sigma_{\text{turb}} = 0.24$ km s^{–1} ($T_{\text{kin}} = 10.3$ K) are found at offsets (–40′′, 160′′) ($\Delta v = 0.54 \pm 0.01$ km s^{–1}) and (–80′′, 0′′) ($\Delta v = 0.590 \pm 0.007$ km s^{–1}), where we observe transonic and supersonic motions with $\mathcal{M}_s = 1.0 \pm 0.1$ and 1.3 ± 0.1 , respectively. However, the latter position reveals an asymmetry of the ammonia magnetic hfs components with a formally deconvolved second subcomponent having a wider linewidth, $\Delta v = 1.26 \pm 0.04$ km s^{–1} (Table A.1). Assuming the same T_{kin} as measured for the main subcomponent, one obtains $\sigma_{\text{turb}} \sim 0.53$ km s^{–1} and $\mathcal{M}_s = 2.8 \pm 0.1$. The velocity dispersion of the weaker subcomponents at two other positions with asymmetric NH₃ lines is of the same order of magnitude, presenting strongly supersonic non-thermal motions at small scales. The regions with asymmetric profiles are probably affected by the closely located IR source IRAS 18264–0143 and protostars at the β and η peaks (see Fig. 4). At all other positions, the dispersions of the random velocity component and the corresponding Mach numbers lie in the intervals 0.05 km s^{–1} $\leq \sigma_{\text{turb}} \leq 0.19$ km s^{–1} and $0.2 \leq \mathcal{M}_s \leq 0.9$, which favors subsonic and transonic motions. Here again, as in the case of SS1, we observe the transition between subsonic and supersonic gas motions occurring over a very short distance $\ell < 0.04$ pc. For example, the narrower component of the NH₃(1, 1) line at offset (–80′′, 0′′)

corresponds to $\mathcal{M}_s = 1.3 \pm 0.1$, whereas at two neighboring positions (–80′′, 40′′) ($\Delta v = 0.28 \pm 0.01$ km s^{–1}) and (–40′′, 0′′) ($\Delta v = 0.26 \pm 0.01$ km s^{–1}), the local Mach numbers are 0.5 ± 0.1 and 0.4 ± 0.2 , which implies $d\sigma_{\text{turb}}/dr \gtrsim 4$ km s^{–1} pc^{–1}.

The deconvolved angular size of the α and β peaks is $124'' \times 45''$ (0.12 pc \times 0.04 pc), which gives the mean diameter ~ 0.07 pc. The gas densities were determined only at the α, β, γ , and δ peaks (Table A.1). Following the same procedure as in Sect. 3.1, the masses of the α and β peaks are $M_\alpha \sim M_\beta = 0.3 M_\odot$. The γ and δ peaks are unresolved; that is, their diameter is less than 0.04 pc. This gives an estimate $M_\gamma, M_\delta < 0.04 M_\odot$. The virial masses of these peaks are $M_{\text{vir}} = 2 M_\odot(\alpha)$, and $1.5 M_\odot(\beta)$, and $M_{\text{vir}} < 0.3 M_\odot(\gamma)$, and $< 0.5 M_\odot(\delta)$. The gas densities at the unresolved ϵ, ζ, θ , and η peaks are not known, so that we can estimate only virial masses: $M_{\text{vir}} < 0.2 M_\odot(\epsilon)$, $M_{\text{vir}} < 0.3 M_\odot(\zeta)$, $M_{\text{vir}} < 1.1 M_\odot(\theta)$, and $M_{\text{vir}} < 5.4 M_\odot(\eta)$.

At the α peak, the total ammonia column density $N(\text{NH}_3) = 9.1 \times 10^{14}$ cm^{–2}, and the gas volume density $n_{\text{H}_2} = 2.7 \times 10^4$ cm^{–3} give the abundance ratio $[\text{NH}_3]/[\text{H}_2] \sim 1.5 \times 10^{-7}$.

3.2.2. SS2B

The serendipitously detected source SS2B is a presumably starless core⁶ curved with a ‘‘C’’ shape. The surface area 82.8 arcmin² at 2 μm of the counterpart #1220 forms approximately a square with side lengths $\sim 550''$ (Fig. 35, panel 43-1 in D11). The dust core completely covers the ammonia emission having a largest extent of $\leq 400''$ and showing five ammonia peaks (Fig. 5). The peaks are labeled α through ϵ in order of decreasing peak line brightness temperature T_{MB} (Table 1). The α and β peaks in the west are just two marginal points along an elongated condensation on the integrated intensity map around the origin (0′′, 0′′) (Fig. 5a). They have practically identical physical parameters (Table A.1) but slightly different radial velocities $V_{\text{LSR}} = 8.19$ and 8.32 km s^{–1}, linewidths $\Delta v = 0.259$, and 0.287 km s^{–1}, and non-thermal velocity dispersions $\sigma_{\text{turb}} = 0.087$ and 0.103 km s^{–1} for the α and β peaks, respectively. The γ -peak located at the eastern side of the C-shaped core with $T_{\text{MB}} = 2.2$ K shows the same brightness temperature as the previously mentioned peaks, whereas its linewidth is 1.5 times larger, $\Delta v = 0.43$ km s^{–1}, and $\sigma_{\text{turb}} = 0.169$ km s^{–1}. The observed linewidths at the δ and ϵ peaks are as narrow as those toward the α and β peaks.

⁵ Saturated emission lines may have ‘‘red shoulders’’ due to self-absorption that are indicative of collapse (e.g., Williams et al. 2006).

⁶ The starless nature of SS2B is deduced from the lack of any IRAS point sources within the boundaries of the core.

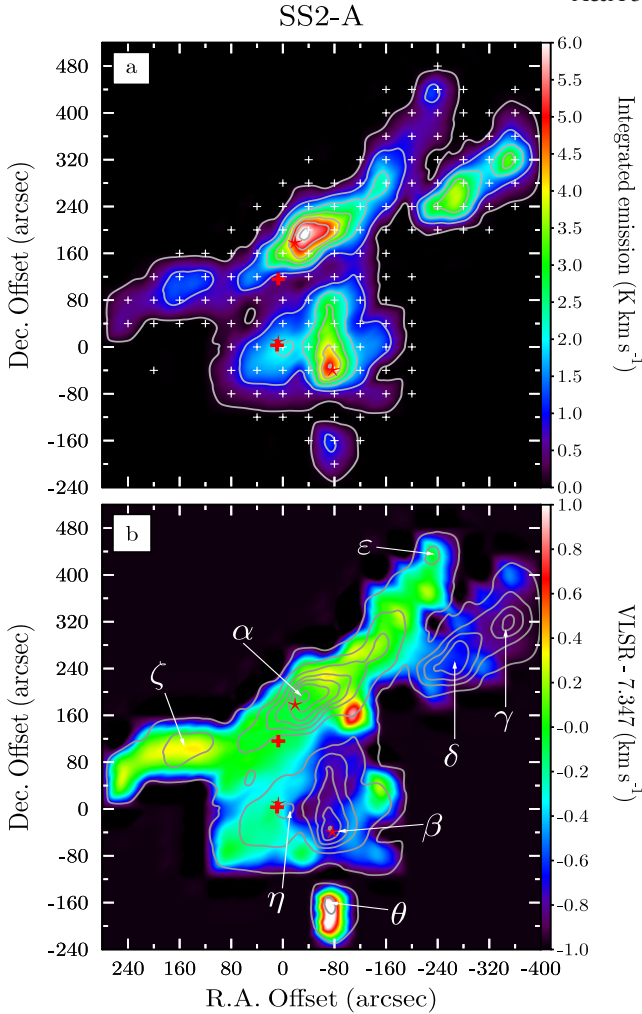


Fig. 4. A zoomed portion of the map shown in Fig. 3. **a)** $\text{NH}_3(1, 1)$ intensity map of SS2A. The starting point for the contour levels is 0.1 K km s^{-1} ; the increment is 0.9 K km s^{-1} between the first two and 1.0 K km s^{-1} between the other contour levels. White crosses mark measured positions, red crosses indicate the location of the IR sources IRAS 18264–0143 and IRAS 18264–0142 (Beichman et al. 1988), and red stars determine Class 0 protostars (Maury et al. 2011). **b)** $\text{NH}_3(1, 1)$ radial velocity field (color map) shown after subtracting the mean radial velocity $\langle V_{\text{LSR}} \rangle = 7.347 \text{ km s}^{-1}$. The ammonia intensity peaks are labeled as in Table 1. The origin of the map position is as in Fig. 3.

The kinetic temperature measured at nine positions toward SS2B is lower on average than that in the two other sources SS1 and SS2A. Moreover, at the offset $(280'', 80'')$, which is close to the γ peak, we detected the lowest kinetic temperature $T_{\text{kin}} = 8.8 \text{ K}$ among T_{kin} listed in Table A.1. The measured values of T_{kin} were used to estimate the dispersion of non-thermal gas motions and the Mach numbers from the observed linewidths. Calculations reveal transonic velocities with $\mathcal{M}_s = 0.9 \pm 0.1$ and 0.8 ± 0.1 at the γ peak ($\Delta v = 0.426 \pm 0.006 \text{ km s}^{-1}$) and at the offset $(80'', 40'')$ ($\Delta v = 0.44 \pm 0.01 \text{ km s}^{-1}$), which are located between the ε and β peaks (see Fig. 5b). At all other positions, we clearly observe subsonic motions with $0.4 \lesssim \mathcal{M}_s \lesssim 0.7$. The positions with the transonic velocities demonstrate a sharp change of the non-thermal velocity dispersion over a distance $\ell \lesssim 0.04 \text{ pc}$. Namely, $d\sigma_{\text{turb}}/dr \gtrsim 2 \text{ km s}^{-1} \text{ pc}^{-1}$ between the β peak and the offset $(80'', 40'')$ and between the γ peak and the narrower NH_3 component at $(280'', 80'')$.

As in the case of asymmetric ammonia profiles discussed in the previous subsection, we detected an asymmetric line

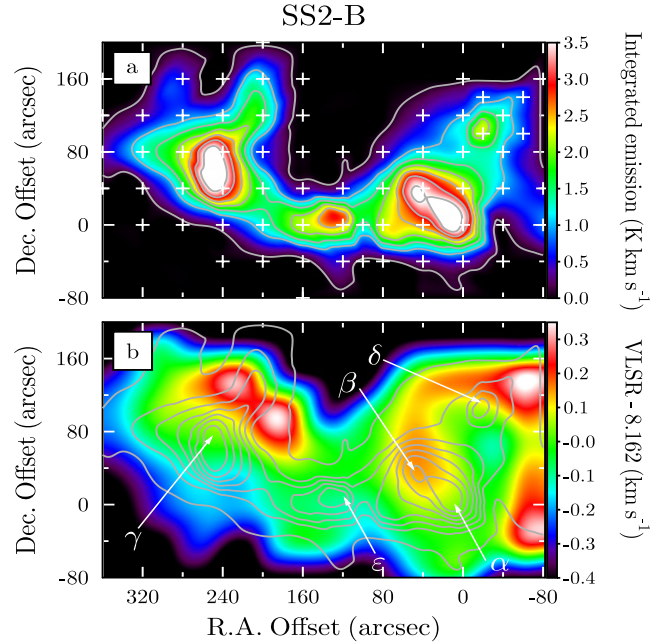


Fig. 5. A zoomed portion of the map shown in Fig. 3. **a)** $\text{NH}_3(1, 1)$ intensity map ($\int T_{\text{MB}} dv$) of SS2B. The starting point for the contour levels is 0.1 K km s^{-1} ; the increment is 0.9 K km s^{-1} between the first two and 0.5 K km s^{-1} between the other contour levels. Crosses mark measured positions. **b)** $\text{NH}_3(1, 1)$ radial velocity field (color map) shown after subtracting the mean radial velocity $\langle V_{\text{LSR}} \rangle = 8.162 \text{ km s}^{-1}$. The ammonia intensity peaks are labeled as in Table 1. The $(0, 0)$ map position is RA = 18:29:47.8, Dec = $-01:37:20$ (J2000).

at the already mentioned offset $(280'', 80'')$ here. This time it shows a blueward asymmetry: this subcomponent is shifted by -0.35 km s^{-1} with respect to the first one (Fig. A.4). Both sub-components are optically thin: for the strongest magnetic hfs component ($F'_1, F' - F_1, F = 2, 5/2 - 2, 5/2$), the optical depths are equal to $\tau = 0.3$ and 0.4 , respectively. Since τ is well below unity, the observed asymmetry must be caused by kinematics rather than radiative transfer effects.

The angular size of the combined $\alpha + \beta$ peak is $120'' \times 120''$ ($0.12 \text{ pc} \times 0.12 \text{ pc}$, $R \sim 0.06 \text{ pc}$). Applying the same procedure as in Sect. 3.1, we find the weighted mean linewidth $\Delta v = 0.28 \text{ km s}^{-1}$, and the mean gas density $n_{\text{H}_2} = 2.2 \times 10^4 \text{ cm}^{-3}$. This gives $M = 1.4 M_{\odot}$ and the virial mass $M_{\text{vir}} = 1.1 M_{\odot}$. The deconvolved angular size of the γ peak $70'' \times 45''$ ($0.07 \text{ pc} \times 0.04 \text{ pc}$, $R \sim 0.03 \text{ pc}$) gives $M = 0.6 M_{\odot}$ and $M_{\text{vir}} \sim 1.8 M_{\odot}$. The structure of the δ and ε peaks is spatially unresolved ($R < 0.02 \text{ pc}$), and their gas densities are not known. In this case, only upper limits on the virial masses can be estimated: $M_{\text{vir}} < 0.3 M_{\odot}(\delta)$, and $< 0.4 M_{\odot}(\varepsilon)$. The ammonia abundance at the resolved $\alpha + \beta$ peak is $X_{\alpha, \beta} \sim 9 \times 10^{-8}$ if the beam filling factor $\eta = 1$.

3.3. L1251C

The object L1251 is a small E-W elongated dark core of the opacity class 5 (the second highest, see Lynds 1962), which is located at a distance $D = 300 \pm 50 \text{ pc}$ (Kun & Prusti 1993). With the coordinates $\ell \approx 115^\circ$, $b \approx 15^\circ$, its distance from the Galactic midplane is about 100 pc . It is a part of the Cepheus Flare giant molecular cloud complex (Lebrun 1986). Five C^{18}O cores embedded in the ^{13}CO cloud were revealed by Sato et al. (1994). The northern core L1251C is one of them. The measured width of the $\text{C}^{18}\text{O}(1-0)$ line toward the peak, as observed with a

beam size of $2''.7$, is $\Delta v = 1.7 \text{ km s}^{-1}$; the radial velocity is $V_{\text{LSR}} = -4.5 \text{ km s}^{-1}$, and the core size is $1.2 \times 0.56 \text{ pc}$ if $D = 300 \text{ pc}$ (Sato et al. 1994). The $2 \mu\text{m}$ emission associated with L1251C was detected toward the dust core #3553 from Dobashi’s catalog (D11). According to D11, $A_V^{\text{core}} = 8.4 \text{ mag}$ at the position of the $2 \mu\text{m}$ peak, and the surface area $S = 233.12 \text{ arcmin}^2$ (angular size $\sim 916''$).

Eight ammonia cores were detected in a map of 0.12 square degrees sampled at intervals of $80''$ (2 times the FWHP) with the Effelsberg 100-m telescope (Tóth & Walmsley 1996). The observed parameters for the northern core L1251C are the following: $N(\text{NH}_3)_{\text{max}} = 8.06 \times 10^{14} \text{ cm}^{-2}$, $n_{\text{H}_2, \text{max}} = 2.6 \times 10^4 \text{ cm}^{-3}$, $V_{\text{LSR}} = -4.79 \text{ km s}^{-1}$, and $\Delta v = 0.30 \text{ km s}^{-1}$ (Tóth & Walmsley 1996).

We mapped the core L1251C in the NH₃(1, 1) and (2, 2) lines with a spacing of $40''$ toward 60 positions marked by crosses in Fig. 6a. This confirms that the NH₃ emission arises from a very compact central region marked by α in Fig. 6b. The third contour level in Fig. 6, corresponding to the half-peak of the integrated emission, $\int T_{\text{MB}} dv$, defines the core size in the NH₃(1, 1) emission line: $a \times b \approx 240'' \times 100''$, which implies $a \times b \approx 0.35 \text{ pc} \times 0.15 \text{ pc}$ if $D = 300 \text{ pc}$.

The results of the fits to the NH₃(1, 1) and (2, 2) spectra are shown by red curves in Fig. A.5, and the estimated physical parameters are given in Table A.2. The excitation temperature T_{ex} is calculated from the (1, 1) transition, assuming a beam-filling factor $\eta = 1$, since both the major and minor axes of the core exceed the angular resolution. We calculated T_{rot} and T_{kin} at all offsets, where both the (1, 1) and (2, 2) transitions were observed (for details, see Appendix A in Paper I). At the core center at offset $(0'', 0'')$, the derived parameters N_{tot} , T_{kin} , and Δv agree with those of Tóth & Walmsley (1996), but we measure a gas density, $n_{\text{H}_2} = 5.9 \times 10^4 \text{ cm}^{-3}$ that is twice as high in value.

The total ammonia column density of $N_{\text{tot}} = 8 \times 10^{14} \text{ cm}^{-2}$ gives the abundance ratio $X = \frac{[\text{NH}_3]}{[\text{H}_2]} = 2 \times 10^{-8}$ at the core center of the mean size $L = \sqrt{a \cdot b} \approx 0.2 \text{ pc}$. The same ammonia abundance was found toward the core SS1 (Sect. 3.1).

The completely resolved ammonia spectra can be used to estimate the contribution of the non-thermal (turbulent) motions to the line broadening. The measured linewidth $\Delta v = 0.290 \pm 0.007 \text{ km s}^{-1}$ and the kinetic temperature $T_{\text{kin}} = 10.5 \text{ K}$ at the core center give a thermal velocity $v_{\text{th}} = 0.10 \text{ km s}^{-1}$, a dispersion of the turbulent motions $\sigma_{\text{turb}} = 0.10 \text{ km s}^{-1}$, a sound speed $c_s = 0.19 \text{ km s}^{-1}$, and a local Mach number $\mathcal{M}_s = 0.5 \pm 0.1$ (see Eqs. (A.6)–(A.10) in Appendix A). Subsonic motions of the non-thermal velocity component are also observed at other positions, where \mathcal{M}_s ranges from 0.3 to 0.6. Thus, the core as a whole gives an example of moderately quiet bulk motions with the ratio of the non-thermal velocity dispersion to the thermal velocity of order unity.

The velocity map of L1251C is shown in Fig. 6b. All along the major axis (E-W direction, $\Delta\delta = -40''$), the radial velocity is close to its mean value $\langle V_{\text{LSR}} \rangle = -4.80 \text{ km s}^{-1}$. In this region, the dispersion of bulk motions is subsonic and roughly constant, $\sigma_{\text{turb}} = 0.12 \pm 0.1 \text{ km s}^{-1}$, which corresponds to $\mathcal{M}_s \approx 0.6$. Such regions are usually called “coherent” (Goodman et al. 1998; Caselli et al. 2002; Pineda et al. 2010)⁷. However, the radial velocity monotonically changes by $\pm 0.2 \text{ km s}^{-1}$ toward the northern and southern edges of the core. As they are attributed to core

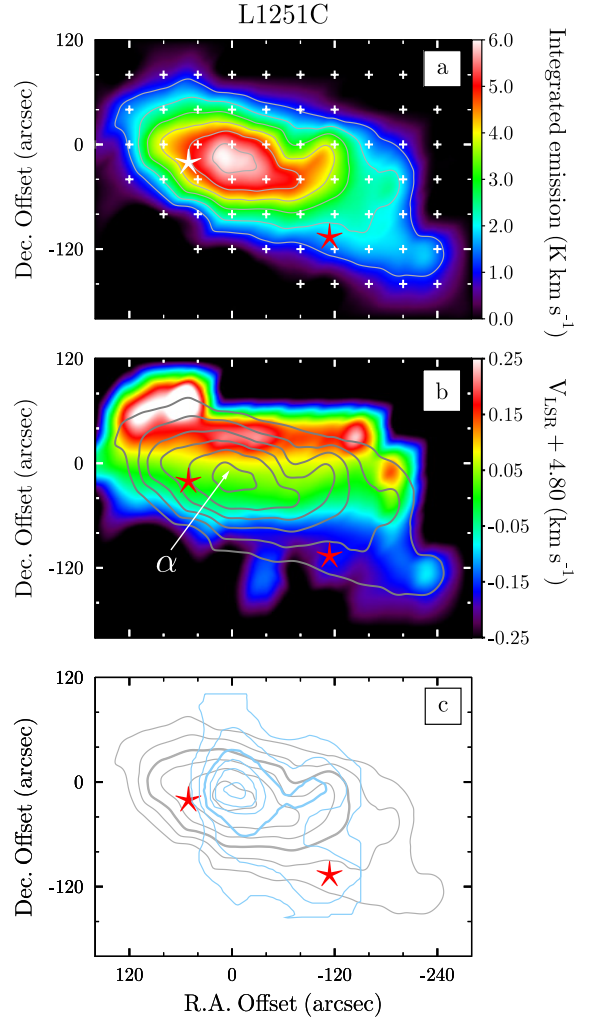


Fig. 6. **a)** NH₃(1, 1) intensity map ($\int T_{\text{MB}} dv$) of L1251C. The starting point for the contour levels is 1.2 K km s^{-1} ; the increment is 0.9 K km s^{-1} . The crosses mark measured positions. The stars indicate the location of the IR sources detected by *IRAS*. **b)** NH₃(1, 1) radial velocity field (color map) shown after subtracting the mean radial velocity $\langle V_{\text{LSR}} \rangle = -4.80 \text{ km s}^{-1}$. The NH₃ peak is labeled as in Table 1. The $(0, 0)$ map position is RA = 22:35:53.6, Dec = 75:18:55 (J2000). **c)** The grey and blue contours show, respectively, the NH₃(1, 1) and N₂H⁺(1–0) intensities integrated over all hyperfine components. The thick contours denote the half-maximum (50%) level, which defines the core size in the corresponding emission line. The N₂H⁺(1–0) data are taken from Fig. 2 of Caselli et al. (2002), where the contour levels are 0.4, 0.7, 1.0, 1.2, 1.5, and 1.8 K km s^{-1} , and the peak intensity is $1.91 \pm 0.12 \text{ K km s}^{-1}$.

rotation, these systematic changes in V_{LSR} correspond to an angular velocity $\dot{\phi} \approx 7 \times 10^{-14} \text{ s}^{-1}$.

For a self-gravitating rigidly rotating sphere of constant density ρ , the ratio of rotational to gravitational binding energy is

$$p = \frac{\dot{\phi}^2}{4\pi G\rho} = 2.55 \times 10^{-3} \dot{\phi}_{-14}^2 / n_4, \quad (1)$$

where G is the gravitational constant, $\dot{\phi}_{-14}$ is the angular velocity in units of 10^{-14} s^{-1} , and n_4 is the gas density in units of 10^4 cm^{-3} (Menten et al. 1984).

Another parameter, which measures the cloud stability, is the ratio between the rotational energy and combined thermal and non-thermal (turbulent) virial terms (e.g., Phillips 1999):

$$p' = 7.04 \times 10^{-2} R^2 \dot{\phi}_{-14}^2 \Delta v^{-2}, \quad (2)$$

⁷ Similar coherent zones were observed in the molecular cores studied in Paper I.

where R is the cloud radius in pc and Δv the linewidth in km s^{-1} . The influence of rotation and turbulence are comparable when the stability parameter $p'(r) \approx 1$.

The calculations show that (i) rotational energy is a negligible fraction of the gravitational energy, $p \approx 0.02$ at the present stage of evolution of L1251C; and (ii) turbulence exceeds the contribution due to rotation in determining cloud stability, $p' \approx 0.4$.

We now compare the NH_3 map with maps of C^{18}O and N_2H^+ . As noted in Sec. 1, CO molecules are usually distributed in larger volumes than NH_3 . This is exactly what we observe in the case of L1251C. Figure 6 shows that the ammonia core has a linear size, which is at least four times smaller, $L_{\text{NH}_3} \approx 0.2$ pc versus $L_{\text{C}^{18}\text{O}} \approx 0.8$ pc. The gas kinematics traced by ammonia differ noticeably from those revealed from C^{18}O : the observed linewidth-size relation $\Delta v_{\text{C}^{18}\text{O}}/\Delta v_{\text{NH}_3} \approx (L_{\text{C}^{18}\text{O}}/L_{\text{NH}_3})^{1.3}$ deviates significantly from the Larson law, $\Delta v \propto L^{0.38}$ (Larson 1981) as established from $^{12}\text{CO}(1-0)$ observations in molecular clouds over a wide range of scales ($\sim 0.05-20$ pc). This may imply that the core is not in perfect virial equilibrium, and its dynamical state is affected by the ambient environment, as found in numerical simulations of turbulent clouds (e.g., Kritsuk et al. 2013).

It is also noteworthy that the $\text{N}_2\text{H}^+(1-0)$ emission is distributed in a smaller area than that of $\text{NH}_3(1,1)$, whereas the peak positions coincide. A direct comparison of the N_2H^+ map of Caselli et al. (2002) with the ammonia map is shown in Fig. 6c. (Both maps were obtained with similar spatial resolutions.) In general, NH_3 and N_2H^+ molecules trace the same volume elements in molecular cores (e.g., Tafalla et al. 2004), because they have a common chemical origin. Nevertheless, our example hints at some chemical differentiation in the process of the dynamical evolution of L1251C.

The mass of the central region, outlined by the thick contour in Fig. 6c, can be estimated using the same procedure as in Sect. 3.1. With the weighted mean linewidth $\Delta v = 0.31$ km s^{-1} , the mean gas density $n_{\text{H}_2} = 3.6 \times 10^4$ cm^{-3} , and the radius $R \sim 0.1$ pc, we have $M = 10.5 M_\odot$ and $M_{\text{vir}} = 2.3 M_\odot$. As in the case of SS1, the observed difference in the masses is probably caused by deviations from a uniform gas density distribution and a core ellipticity.

4. Autocorrelation and structure functions

4.1. General considerations

In this Section, we focus on the character of the observed stochastic motions of the gas mapped in ammonia emission. Taking a low fractional abundance of NH_3 ($X \lesssim 10^{-7}$) into account, the question arises whether the ammonia emission traces the gas distribution. In what follows, we assume that the answer is positive. To support this assumption, we note that ammonia and submillimeter maps of dense cores show a close correlation between the large-scale distributions of the $\text{NH}_3(1,1)$ integrated intensity and the continuum emission, as was pointed out in Sect. 3 and discussed in Friesen et al. (2009). Since dense cores are mostly composed of molecular gas ($\sim 77\%$ of H_2 , and $\sim 23\%$ of He by mass, neglecting metals), we may consider ammonia as a passive heavy impurity, which does not perturb dynamics of the gas motion. We suppose that the ammonia impurity is conservative, that is, the relative abundance of NH_3 does not change when moving from one point to another within the core.

Stochastic motion can be scale-free (purely random) or characterized by some length scale(s). In particular, turbulence is a

stochastic motion with multiple scales. An essential feature of turbulence is a swirling motion, which is viewed as eddies of various sizes. The size of largest eddies is comparable with the physical dimension of the flow (in our case – of the molecular cloud itself), whereas a lower limit on the size of eddies is of the order of the molecular mean free path. That is, for a dense core it is $\lambda = (\sqrt{2}n\sigma)^{-1} \sim 10^{-7}$ pc (the effective cross section $\sigma \sim 10^{-15}$ cm^2 , the gas density $n \sim 10^4$ cm^{-3}). Actually, the size of the smallest eddies is determined by viscosity, which prevents the formation of eddies at lower scales. At this limit, the turbulent motion is converted into thermal intermolecular energy, which is then dissipated into the ambient medium. The current paradigm regards turbulent flows as an energy cascade, where the kinetic energy is injected at large scales and is then transferred to smaller scales by various nonlinear processes. The model of energy cascade for the simplest case of the incompressible turbulent flow was first developed by Kolmogorov (1941). In reality, the energy transfer is a rather complicated process. It is known to be highly intermittent at small scales due to the process of stretching of vortex filaments (e.g., Lesieur 1997). Another important property is the multifractality of the kinetic energy dissipation field characterized by many scaling indices (e.g., Sreenivasan 1991).

To quantitatively describe the multiscale properties of the stochastic motions, different methods are used including calculations of the two-point autocorrelation function (ACF) of the random velocity field, the structure function (SF), and the power spectrum (PS), which is the frequency-space analog of the ACF (e.g., Kaplan & Klimishin 1964; Scalo 1984; Dickman & Kleiner 1985; Miesch & Bally 1994; Lagrois & Joncas 2011).

In what follows, we assume that the turbulent velocity field is homogeneous, where the mean LSR radial velocity is constant within the NH_3 area and isotropic; that is, the ACF and SF depend only on the distance between two positions on the plane of the sky, ($\vec{r} = |\mathbf{r}_1 - \mathbf{r}_2|$). In this case, the normalized autocorrelation and structure functions are given by (e.g., Yaglom 1987):

$$B(\vec{r}) = \frac{\sum [V_c(r) - \mu][V_c(r + \vec{r}) - \mu]}{\sigma_c^2 N(\vec{r})}, \quad (3)$$

and

$$D(\vec{r}) = \frac{\sum [V_c(r) - V_c(r + \vec{r})]^2}{\sigma_c^2 N(\vec{r})}. \quad (4)$$

Here, $N(\vec{r})$ is the number of pairs at each lag \vec{r} . The summation in (3) and (4) is over $N(\vec{r})$ pairs. V_c ($\equiv V_{\text{LSR}}$), as defined in Eq. (A.4), is the mean radial velocity of the emitting gas averaged over the line-of-sight and given by the velocity centroid of the $\text{NH}_3(1,1)$ line. The parameter μ is the mean centroid velocity:

$$\mu = \frac{\sum V_c(r)}{N}, \quad (5)$$

and σ_c^2 is the variance of centroid velocity fluctuations:

$$\sigma_c^2 = \frac{\sum [V_c(r) - \mu]^2}{N}. \quad (6)$$

The total number of the velocity centroids in the map is N .

For homogeneous fields, $B(\vec{r})$ and $D(\vec{r})$ are related as (Yaglom 1987):

$$D(\vec{r}) = 2[1 - B(\vec{r})]. \quad (7)$$

From Eq. (3), it follows that $B(\vec{r}) \rightarrow 1$ at $\vec{r} \rightarrow 0$. With increasing \vec{r} , the velocities become uncorrelated and $B(\vec{r}) \rightarrow 0$ at $\vec{r} \rightarrow \infty$.

Correspondingly, $D(\tilde{r}) \rightarrow 2$ at $\tilde{r} \rightarrow \infty$, and $D(\tilde{r}) \rightarrow 0$ at $\tilde{r} \rightarrow 0$. Sometimes, Eq. (7) is used to justify homogeneity of the turbulent field (e.g., Kitamura et al. 1993). If the calculated values of ACF and SF are related in accord with (7), then the field is considered homogeneous. However, it is not proven mathematically, and, hence, the statement is ambiguous.

As mentioned above, the ACF and PS provide the same information on the stochastic properties of the turbulent flow. For isotropic turbulence, the power spectrum $P(k)$ is a function of the wavenumber $k = 1/\tilde{r}$:

$$P(k) = \frac{1}{2\pi} \int_{-\infty}^{\infty} e^{-ik\tilde{r}} B(\tilde{r}) d\tilde{r}. \quad (8)$$

In the inertial range of the developed turbulence – between the energy input and dissipation scales, the PS may be approximated by a single power law with a spectral index κ , $P(k) \propto k^{-\kappa}$. Often observed for the cold ISM are 3D spectra with $\kappa_{3D} \approx 3.6$ (note that for angle-averaged 1D spectra $\kappa_{1D} = \kappa_{3D} - 2$), which is consistent with the Kolmogorov's scaling of incompressible turbulence, $P_{3D}(k) \propto k^{-11/3}$ (e.g., Falgarone et al. 2007). In this case, the ACF is a monotonic function asymptotically approaching zero at large lags.

In practice, the calculated value of the ACF, $\zeta = B(\tilde{r})$, is affected by statistical errors. We estimate the 1σ confidence interval for ζ with the aid of the Fisher transformation:

$$f(z) = \frac{1}{2} \ln \frac{1+z}{1-z} = \operatorname{arctanh}(z). \quad (9)$$

The function $f(z)$ approximately follows a normal distribution with a mean $m = f(\zeta) = \operatorname{arctanh}(\zeta)$ and the standard error $\sigma_z = 1/\sqrt{N-3}$, where N is the sample size. Calculated in the transformed scale, the 1σ confidence interval ($f_1 = m - \sigma_z$, $f_2 = m + \sigma_z$) was converted back to the correlation scale

$$z(f) = \frac{e^{2f} - 1}{e^{2f} + 1} = \tanh(\operatorname{arctanh}(z)), \quad (10)$$

yielding the 1σ confidence interval for each ζ .

4.2. ACFs for molecular cores

The calculated values of ACF and SF are not statistically reliable at large lags, where the sample sizes are small, mainly due to irregular boundaries of the core and the lack of measurements outside of it. In our observations, the angular sizes of the NH₃ areas are not sufficiently large ($\lesssim 10' \times 10'$) compared with the angular resolution ($FWHP = 40''$). Therefore, to improve statistics, we averaged the ACFs and SFs over an azimuthal angle, assuming isotropy, as was usually done in previous studies (e.g., Scalo 1984; Kitamura et al. 1993; Miesch & Bally 1994) and calculated one-dimensional functions $B(\tilde{r})$ and $D(\tilde{r})$. Following Dickman & Kleiner (1985) and Miesch & Bally (1994), these functions were corrected at nonzero lags for instrumental noise, giving rise to a velocity centroid variance σ_{rms} . However, a typical value of $\sigma_{\text{rms}} \sim 0.02 \text{ km s}^{-1}$ and the standard deviation of centroid velocity fluctuations $\sigma_c \sim 0.2 \text{ km s}^{-1}$ show that the correction factor $1 - (\sigma_{\text{rms}}/\sigma_c)^2 \sim 1$ and, thus, the influence of the instrumental noise on the ACF is negligible.

The profiles of the azimuthally averaged autocorrelation function $B(\tilde{r})$ and structure function $D(\tilde{r})$ are shown in Fig. 7, where the latter is plotted in the form $1 - D(\tilde{r})/2$ for the comparison with the former. The cores were selected from both the

current study and Paper I based on velocity maps having a sufficiently large number of observed positions to decrease the statistical noise. The scatter of the points plotted in Fig. 7 is mainly due to the statistical errors: it decreases with increasing numbers of data points. We simply cut the ACF profiles at large lags if the scatter becomes too large, $|B(\tilde{r})| \gtrsim 1$. Figure 7 shows a formal concordance between the ACF and SF values; to analyze turbulence in molecular cores, we mostly use the ACFs.

The ACF gives us information on the characteristic scales of the turbulent energy spectrum. In particular, the correlation length, ℓ_c , is a spatial scale corresponding to the lag where the ACF falls down to $1/e$, $B(\ell_c) = e^{-1}$. If the turbulent structure of a core is completely resolved in observations, or the correlation length is larger than the beamwidth, then the true correlation length of the velocity field can be estimated. However, spurious correlations may occur in the velocity field due to beam smoothing in the case of partially resolved or unresolved observations. The relation between the apparent velocity correlation length, ℓ_a , the true correlation length, ℓ_c , and the Gaussian beam width, θ , of a radio telescope is given by (Kitamura et al. 1993):

$$\ell_a^2 = \ell_c^2 + \theta^2 / \ln 4, \quad (11)$$

which predicts for our ammonia observations $\ell_a \approx 34''$ ($\sim 0.02 \text{ pc}$) induced solely by the beam smoothing if the velocity scale of the underlying motion is unresolved, $\ell_c \ll \theta$.

The scale ℓ_0 , where the correlation vanishes, $B(\ell_0) = 0$, is another important parameter provided by ACFs. One may consider ℓ_0 as a typical size of the largest energetic turbulence fluctuations (e.g., Miville-Deschênes et al. 1995).

The plots in Fig. 7 reveal three types of apparent ACF profiles: (1) spikelike at the origin as seen for the source SS3; (2) partially resolved with $\ell_a \sim \theta$ (Do279P6, SS2B, Do321P2, SS1, Ka01, Do279P7), and (3) resolved with $\ell_a > \theta$ (SS2A, Do279P12, L1251C). Besides, seven ACFs have ranges with statistically significant negative correlations: SS2A, Do279P12, Do321P2, SS1, L1251C, Ka01, and Do279P7.

The spikelike ACF of SS3 reflects a purely random motion with an uncorrelated velocity field (white noise process). The core itself is located in the active star-forming region Serpens South, harboring a number of young stellar objects (YSOs). It exhibits a complex velocity field structure, and asymmetric ammonia lines (Figs. 10 and B.8 in Paper I). However, an even higher star-formation activity and asymmetric NH₃ lines are observed toward, for example, Do279P12 (Figs. 4 and B.4 in Paper I), where the presence of characteristic correlation scales is quite evident (Fig. 7). Such a contrast between the velocity fields in similar objects with $\mathcal{M}_s \sim 1.5$ for both of them is surprising, since it is assumed that turbulence is a universal property of most of the molecular gas in the Milky Way from giant molecular clouds down in size to compact cores (McKee & Ostriker 2007).

For partially resolved ACFs, we calculated the following apparent correlation lengths: $\ell_a \approx 40''$ (Do321P2, SS1, Ka01), $\ell_a \approx 50''$ (Do279P7), and $\ell_a \approx 60''$ (Do279P6, SS2B). The values corrected for beam smoothing are: $\ell_c \lesssim 0.02 \text{ pc}$, $\ell_c \sim 0.04 \text{ pc}$, and $\ell_c \sim 0.05 \text{ pc}$, respectively. The first zero crossing occurs at $\ell_0 \sim 0.06 \text{ pc}$ (SS1, Do279P7), $\ell_0 \sim 0.08 \text{ pc}$ (Do321P2), $\ell_0 \sim 0.09 \text{ pc}$ (Ka01), $\ell_0 \sim 0.16 \text{ pc}$ (SS2B), and $\ell_0 \sim 0.24 \text{ pc}$ (Do279P6).

All spatially resolved ACFs (SS2A, L1251C, Do279P12) show the correlation length $\ell_c \sim 0.1 \text{ pc}$, whereas ℓ_0 is ~ 0.13 , ~ 0.15 , and $\sim 0.18 \text{ pc}$, respectively.

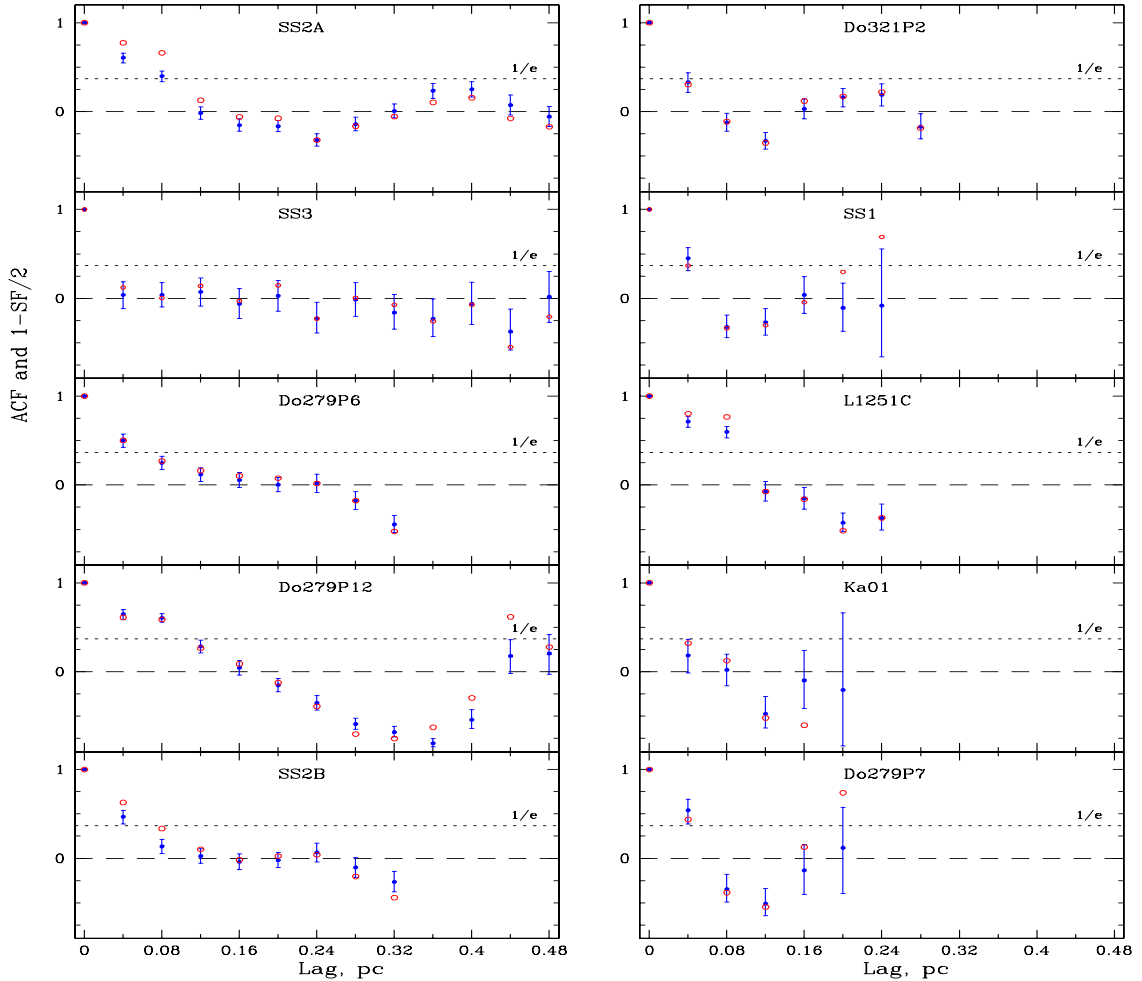


Fig. 7. Azimuthally averaged autocorrelation functions (ACFs) plotted by blue dots with 1σ error bars and azimuthally averaged structure functions (SFs) plotted by red open circles for the NH_3 turbulent velocity fields. For the SFs, the values $(1 - \text{SF}/2)$ are shown to check homogeneity of the velocity map in accord with Eq. (7). The error bars for the $(1 - \text{SF}/2)$ points are the same as for the ACFs. The zero and $1/e$ levels are shown by long- and short-dashed lines. The sources Do279P6, Do279P7, Do279P12, Do321P2, Ka01, and SS3 are from Paper I, while SS1, SS2A, SS2B, and L1251C are from the present paper.

4.3. Oscillating ACFs

An interesting feature detected in about 70% of ACFs of the NH_3 velocity maps is the presence of ranges with statistically significant negative correlation. This type of ACF deserves an additional discussion. We calculate ACFs based on maps obtained directly from NH_3 profile measurements and under assumptions of spatial homogeneity and isotropy of the underlying velocity field. However, it is known that slow drifts in the mean values of the stochastic field and/or anisotropy can significantly distort the ACF, eventually producing regions of negative correlations (Yaglom 1987). If we are interested in revealing the true statistical properties of the stochastic field, then such bulk motions should be removed. In practice, this occurs by filtering the measured maps with an appropriate window, the size of which is determined in a series of consecutive trials (e.g., Lagrois & Joncas 2011). Unfortunately, this method is not applicable due to a low number of points in the maps in our case, so that the filtering with a large window becomes equivalent to a simple subtraction of the mean value of V_{LSR} . Nevertheless, there is a possibility to test the effects of bulk motions on the ACF even with our limited maps, namely, by comparing the ACFs calculated for two different directions.

In the present sample, we have one object L1251C where the presence of the large-scale velocity gradient in the N-S direction across the whole surface area is clearly visible (Fig. 6b). Figure 8 shows ACFs calculated along the velocity gradient, $B_{\text{N-S}}$, and perpendicular to it, $B_{\text{E-W}}$. The autocorrelation function $B_{\text{N-S}}$ decreases monotonically becoming negative at $\tilde{r} \gtrsim 0.08$ pc, whereas $B_{\text{E-W}}$ is everywhere positive. On the other hand, cores SS2A, Do279P12, and Do321P2 do not demonstrate signs of large-scale motion. For them, both the azimuthally averaged ACF and the direction-based values $B_{\text{N-S}}$ and $B_{\text{E-W}}$ show similar behavior with oscillations damped with increasing lags (Fig. 8). Thus, we may conclude that for these three cores the assumption of isotropy is valid and that the damping oscillations indicate a real small-scale structure of the velocity field in the dense cores.

Oscillating ACF are usually detected in atmospheric turbulence (Yaglom 1987); in astrophysics, a similar shape of the azimuthally averaged ACF was reported for dense cores in the Milky Way by Kitamura et al. (1993), where $4' \times 4'$ and $8' \times 8'$ areas toward the core TMC-1C in Heiles' cloud 2 of the Taurus complex were mapped in the $^{13}\text{CO}(1-0)$ and $\text{C}^{18}\text{O}(1-0)$ lines. Those observations were carried out at the Nobeyama 45 m telescope with an angular resolution $FWHP \approx 17''$ (0.01 pc). As for extragalactic objects, oscillating ACFs were observed in two

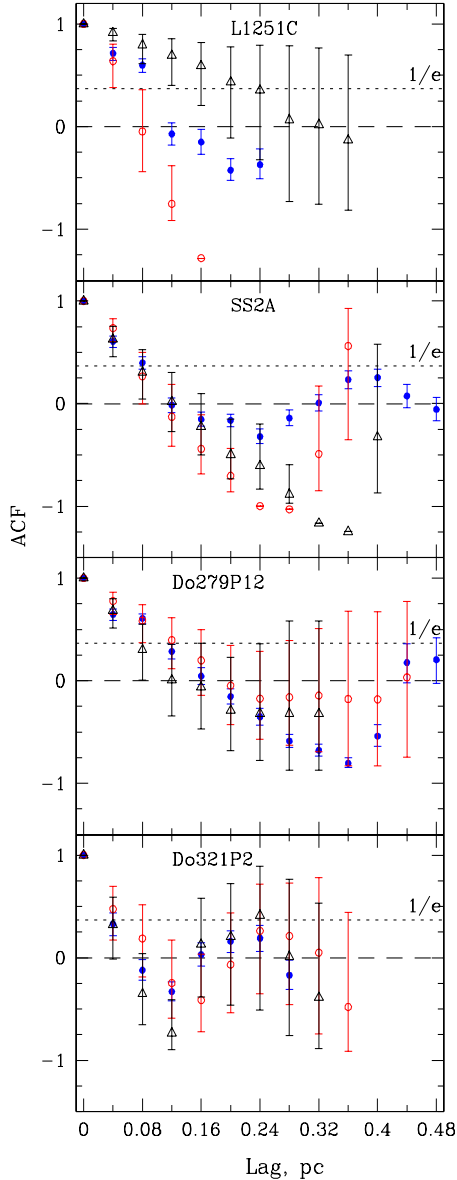


Fig. 8. Testing the isotropy of the observed velocity field. Blue dots show azimuthally averaged autocorrelation functions (ACFs), as already plotted in Fig. 7, whereas ACFs calculated for directions N→S and E→W are shown by red open circles and black open triangles, respectively. Error bars show 1σ statistical errors. At large lags due to poor statistics, some points without error bars have a formal value $|\text{ACF}| \geq 1$, and therefore, their errors cannot be defined using Eq. (9). In *panel L1251C*, a large-scale gradient of the velocity field (see Fig. 6b) manifests itself as a monotonically decreasing ACF with increasing lags in the direction of the velocity gradient and as positive correlations for perpendicular direction. Both N-S and E-W ACFs deviate significantly from the azimuthally averaged ACF. On the other hand, panels SS2A, Do279P12, and Do321P2 show similar damping oscillations for all three ACFs, as expected, if the velocity field is homogeneous and isotropic.

giant H II regions NGC 604 and NGC 595 in M33 by Medina Tanco et al. (1997) and Lagrois & Joncas (2011), respectively.

In fluid dynamics, a similar behavior of the velocity ACF predicted for a so-called Lennard-Jones fluid in which the interaction between a pair of flow particles is governed by the interplay of the short-range repulsive and the long-range attractive forces (e.g., Wijeyesekera & Kushick 1979; Lad & Pratap 2004).

Forces acting in molecular cores may be considered in a similar manner: gravity generating the infall motion is an attractive force, whereas forces that provide support against gravitational collapse – centrifugal, dissipative and magnetic – are repulsive.

To describe the shape of the fluctuating ACF, we employ a model of damping oscillation that is often used to represent empirical correlation functions, which alternate between positive and negative values (Yaglom 1987):

$$\tilde{B}(\tilde{r}) = e^{-\gamma\tilde{r}}[\cos(a\tilde{r}) + \xi \sin(a\tilde{r})]. \quad (12)$$

The choice of this model, which is by no means unique, is determined by its simplicity and by the gravitational potential within a spherically symmetric mass distribution that behaves like $\propto r^2$. Just for this type of potential, the ACF in the form of (12) was deduced for a Brownian particle diffusion in a harmonic well (Glass & Rice 1968). The parameters γ and a in (12) are defined in the spatial domain and, thus, are measured in pc^{-1} ; the parameter ξ is a dimensionless quantity. The autocorrelation function $\tilde{B}(\tilde{r})$ is normalized to unity at lag $\tilde{r} = 0$.

If the curve defined by Eq. (12) closely fits experimental data, we can replace the empirical ACF by an analytical function $\tilde{B}(\tilde{r})$ and, hence, use it to determine the power spectrum also analytically. The Fourier transform, Eq. (8), of $\tilde{B}(\tilde{r})$ gives

$$P_{\text{1D}}(k) = \frac{1}{\pi} \frac{c_1 + c_2 k^2}{c_3 + c_4 k^2 + k^4}, \quad (13)$$

where $c_1 = \gamma^3 + \gamma a^2 + \xi a \gamma^2 + \xi a^3$, $c_2 = \gamma - \xi a$, $c_3 = (a^2 + \gamma^2)^2$, $c_4 = 2(\gamma^2 - a^2)$, and $P_{\text{1D}}(k) \propto k^{-2}$ at large k .

The Kolmogorov model of the velocity field in incompressible turbulence postulates a dissipationless cascade characterized in the inertial range by a transfer rate of kinetic energy independent of scale. In this model, the PS of the velocity $P_{\text{1D}} \propto k^{-5/3}$. On the other hand, the spectrum of a highly compressible medium should scale at high Mach numbers as k^{-2} (e.g., Passot et al. 1988), which was confirmed in numerical simulations by Kritsuk et al. (2007). One sees that the function defined by Eq. (13) has the same asymptotic behavior at large wavenumbers.

Below we consider the velocity field characteristics of three cores with oscillating ACFs in more detail employing the model (12) to fit their empirical ACFs to estimate the model parameters γ , a , and ξ .

4.3.1. SS2A

The Aquila target SS2A exhibits a highly perturbed velocity field (Sect. 3.2.1) along with gas density variations (Table A.1). It contains an IR source and a few protostars, which generate gas outflows seen from the enhanced linewidths of NH₃ in the vicinity of these sources. No clear features of a rigid-body rotation of the core as a whole or any significant large-scale gradients of the velocity field are found.

Figure 9a shows the best fit of the model curve (solid line) to the measured velocity correlation function (filled circles with 1σ error bars). In panel b, the corresponding PS given by Eq. (13) with the estimated model parameters $\gamma \simeq 6 \text{ pc}^{-1}$, $\xi \simeq 0.2$ and $a \simeq 15 \text{ pc}^{-1}$ is plotted. For comparison, a pure Kolmogorov cascade of incompressible turbulence (dashed line) with a scaling $\propto k^{-5/3}$ is also presented. The PS of SS2A forms a noticeable knee at $k_m \approx 17 \text{ pc}^{-1}$. In general, three ranges in the model PS shape can be distinguished: the environmental ($k < k_m$), driving ($k \approx k_m$), and inertial/dissipative

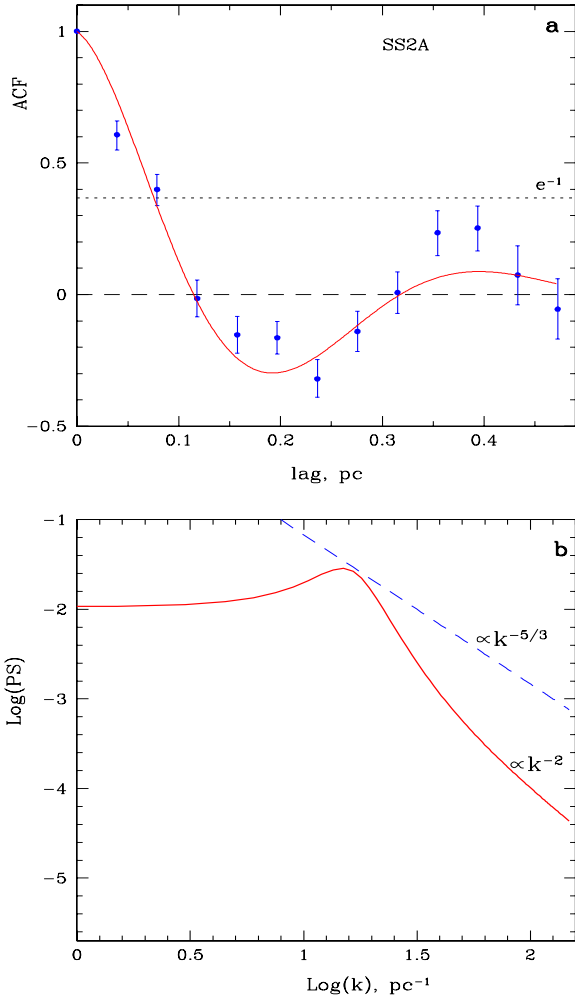


Fig. 9. Autocorrelation function (ACF) and corresponding power spectra (PS) of the turbulence in SS2A. **a)** The solid line indicates the best fit of the azimuthally averaged ACF (filled circles with 1σ error bars) to a model of decaying oscillations as discussed in Sect. 4.3. The zero and e^{-1} levels are shown by long- and short-dashed lines. The lag \bar{r} is given in pc for the distance to the source $D = 203$ pc. **b)** The power spectrum of velocity $P_{1D}(k)$ (solid line) assumes homogeneous and isotropic turbulence (the wavenumber $k = 1/\bar{r}$). The spectrum is calculated using Eq. (13). Note the turnover of the PS at a scale of ≈ 0.06 pc ($k_m \approx 17$ pc $^{-1}$), where energy is being injected into the system. For comparison, the theoretical PS of a pure Kolmogorov cascade of incompressible turbulence is shown by a dashed line. The Kolmogorov power-law index is $\kappa_{1D} = -5/3$, while the model value is -2 in the inertial range at high wavenumbers, $k > k_m$.

PS ($k \gtrsim k_m$)⁸. In the environmental range (at large scales), the model shows a flat spectrum at different wavenumbers. The energy is injected into the gas motion at $k \sim k_m$ ($\ell_m \sim 0.06$ pc) and is dissipated at scales $k > k_m$. The model ACF drops to the level of $1/e$ at $\ell_c = 0.08$ pc (Fig. 9a).

4.3.2. Do279P12

The source Do279P12 is a dark core with numerous embedded YSOs, IR and Herbig-Haro objects along with

⁸ We note that the meaning of the inertial range is applicable to a well developed turbulence, which is characterized by statistical regularities over a wide range of scales. This may not be the case, however, for a compact dark core subjected to self-gravitation.

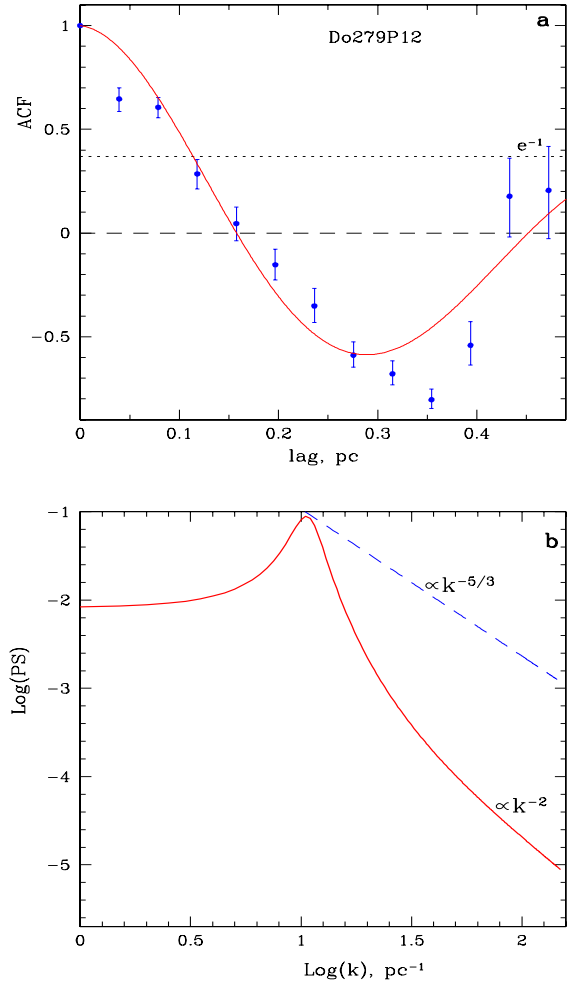


Fig. 10. Same as Fig. 9 but for the source Do279P12.

submm-continuum and radio sources (Fig. 4 in Paper I). The ammonia lines show a double component structure toward a few offsets (Figs. 6 and B.4 in Paper I). We interpreted this splitting as a purely kinematic effect since it is present in the optically thin NH_3 lines as well. Both core SS2A and Do279P12 have similar linear sizes and the morphology of the $\text{NH}_3(1,1)$ map: an elongated surface of irregular form.

The correlation length $\ell_c \approx 0.12$ pc (Fig. 10a) is well defined, thus suggesting a highly structured velocity field. The ACF shows a decaying oscillation in the range (0.16, 0.5) pc with a prominent negative region between 0.16 pc and 0.44 pc, while the corresponding PS (Fig. 10b) exhibits a sharp peak at $k_m \approx 11$ pc $^{-1}$ ($\ell_m \approx 0.09$ pc), which is of the order of the sonic length, $\ell_s \sim 0.1$ pc. The estimated model parameters are $\gamma \approx 1.8$ pc $^{-1}$, $a \approx 11$ pc $^{-1}$, and $\xi \approx 0.1$.

4.3.3. Do321P2

The ACF profile of Do321P2 and those shown in the right panels of Fig. 7 (SS1, Ka01, and Do279P7) are only partially resolved and affected at small scales by beam smoothing. However, their ACFs demonstrate statistically significant negative correlations resembling those measured in SS2A and Do279P12 at larger scales. The object Do321P2 has a larger angular size, and, thus, its ACF was measured more accurately.

The object Do321P2 is a filamentary dark core with a few YSOs, SCUBA, and IRAS sources embedded (Fig. 7 in Paper I).

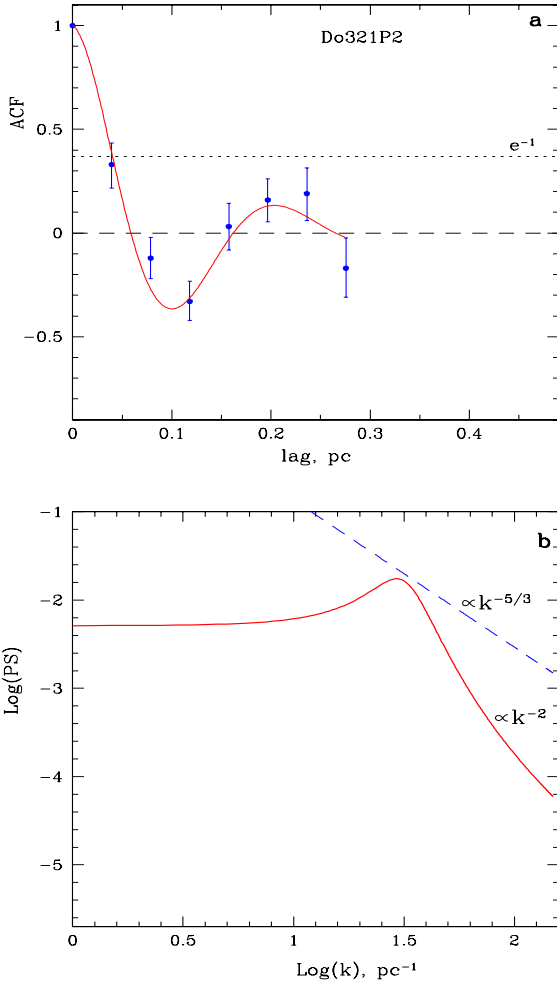


Fig. 11. Same as Fig. 9 but for the source Do321P2.

The NH₃ velocity map (Fig. 7b in Paper I) shows an irregular structure with distinct pockets of redshifted and blueshifted ammonia emission around the clusters of YSOs. The observed kinematics are caused by large-scale motions in this star-forming region.

The azimuthally averaged ACF of the velocity field is shown in Fig. 11a by filled circles with 1σ error bars. The smooth line represents the model ACF. The estimated model parameters are $\gamma \simeq 9.8 \text{ pc}^{-1}$, $a \simeq 30.4 \text{ pc}^{-1}$, and $\xi \simeq 0.2$. In panel b, the PS is shown. The model results may be affected by beam effects, and caution must be taken in prescribing them any significance. Higher angular resolution observations are required to get reliable physical parameters of the bulk motion in this and in the above mentioned cores showing similar properties (SS1, Ka01, and Do279P7).

5. Summary

We have used the Effelsberg 100-m telescope to map NH₃(1, 1) and (2, 2) toward three dark cores in the Aquila rift cloud complex (SS1, SS2A, B) and toward one core in the Cepheus molecular cloud (L1251C). The Aquila targets were preliminary selected from the CO, ¹³CO, and C¹⁸O survey carried out with the Delingha 14-m telescope (Wang, priv. comm.). The Cepheus target was delineated from the C¹⁸O map by Sato et al. (1994).

The observed ammonia cores demonstrate complex intrinsic motions and fluctuating gas density and kinetic temperature on

the scales $0.04 \lesssim \ell \lesssim 0.5 \text{ pc}$. The amplitude of the gas density fluctuation is $(n_{\text{H}_2})_{\text{max}}/(n_{\text{H}_2})_{\text{min}} = 2$ and 4 for, SS1 and SS2A, respectively, and it is up to 5 for both SS2B and L1251C, while the mean density in these core is $\langle n_{\text{H}_2} \rangle / 10^4 = 2.4, 1.8, 1.7,$ and 3.6 cm^{-3} , respectively (Tables A.1, A.2). The measured ammonia abundances, $X = [\text{NH}_3]/[\text{H}_2]$, vary between $X = 2 \times 10^{-8}$ (SS1 and L1251C) and $X = 10^{-7}$ (SS2A, B).

A systematically higher kinetic temperature is measured in cores harboring YSOs (SS1, SS2A, L1251C) as compared to the starless object SS2B: a maximum $T_{\text{kin}} \simeq 15 \text{ K}$ for the former versus maximum $T_{\text{kin}} \simeq 11 \text{ K}$ for the latter. The minimum $T_{\text{kin}} = 8.8 \text{ K}$ is detected in SS2B as well.

The measured kinetic temperature was used to estimate the line of sight dispersion of the non-thermal bulk motions from the observed linewidths. We found that the Cepheus core differs noticeably with respect to this parameter from the Aquila sources. A quiet gas motion with $\sigma_{\text{turb}} \sim v_{\text{th}}$ is observed toward L1251C, while the velocity fields are highly perturbed in Aquila. The two Aquila cores SS1 and SS2A have internal regions where the Mach number $\mathcal{M}_s > 1$ and the velocity dispersion changes with a high rate of $d\sigma_{\text{turb}}/dr \gtrsim 4 \text{ km s}^{-1} \text{ pc}^{-1}$. The third core SS2B with $\mathcal{M}_s < 1$ has two regions where $d\sigma_{\text{turb}}/dr \gtrsim 2 \text{ km s}^{-1} \text{ pc}^{-1}$. However, $d\sigma_{\text{turb}}/dr \approx 0 \text{ km s}^{-1} \text{ pc}^{-1}$ for L1251C where $\mathcal{M}_s < 1$ as well.

The object L1251C is also the only core among those analyzed in this paper where a regular velocity gradient with respect to the central ‘‘coherent’’ velocity zone is observed. When interpreted as rigid-body rotation, this gives an angular velocity $\dot{\phi} \approx 7 \times 10^{-14} \text{ s}^{-1}$. However, the corresponding rotational energy is a negligible fraction of the gravitational energy, since the parameter p in Eq. (1) is $\ll 1$. In the same way, a significant deviation from Larson’s law ($\Delta v \propto L^{1.3}$ instead of $\propto L^{0.38}$) indicates a decreasing contribution of the turbulent energy to core stability. Another distinct feature of this core is the noncongruent maps of NH₃ and N₂H⁺ emission showing that these molecules do not trace exactly the same region and that the latter is concentrated within a smaller volume surrounding the central gas density peak NH₃(1, 1).

Masses from one to ten M_{\odot} are estimated for SS1 and L1251C, whereas they are $\lesssim M_{\odot}$ for the α and β peaks in SS2A and SS2B, and significantly less than the solar mass for other ammonia peaks in these cores.

We present new examples of the ACF of the velocity field with slowly decaying oscillations on scales $\sim 0.04\text{--}0.5 \text{ pc}$. The corresponding PS deviates significantly from a single power-law cascade and exhibits a knee in its shape. Such a kind of the PS may arise at a transient stage of the dynamic evolution of a dense core when self-gravity directly competes with the nonconservative forces. We suggest that oscillating ACFs may indicate a damping of the developed turbulent flows surrounding the dense but less turbulent core, a transition to dominating gravitational forces and, hence, to gravitational collapse.

To conclude, we would like to emphasize that the reliability of damping oscillations requires further confirmations from higher angular resolution observations and better statistics while the damping oscillations in the ACF may reflect a particular turbulent structure of the dense cores. The study of Aquila dense cores will be continued with the Effelsberg 100-m telescope to further investigate their physical and kinematic properties.

Acknowledgements. We thank the staff of the Effelsberg 100-m telescope for their assistance in observations, and we appreciate Alexei Kritusk’s and Andrei Bykov’s comments on an early version of the manuscript. We also thank the anonymous referee for suggestions that led to substantial improvements of the paper. S.A.L. is grateful for the kind hospitality of the Max-Planck-Institut für

Radioastronomie and Hamburger Sternwarte where this work has been prepared. This work was supported in part by the grant DFG Sonderforschungsbereich SFB 676 Teilprojekt C4, and by the RFBR grant No. 14-02-00241.

References

- André, P., Di Francesco, J., Ward-Thompson, D., et al. 2013, in *Protostars and Planets VI* (University of Arizona Press), in press
[arXiv:astro-ph/1312.6232]
- Beichman, C. A., Neugebauer, G., Habing, H.J., Clegg, P. E., & Chester, T. J. 1988, *NASA Ref. Publ.*, 1190, 1
- Caselli, P., Benson, P. J., Myers, P. C., & Tafalla, M. 2002, *ApJ*, 572, 238
- Churchwell, E., Walmsley, C. M., & Cesaroni, R. 1990, *A&AS*, 83, 119
- Crutcher, R. M. 2012, *ARA&A*, 50, 29
- Dickman, R. L., & Kleiner, S. C. 1985, *ApJ*, 295, 479
- Dobashi, K. 2011, *PASJ*, 63, S1 (D11)
- Dobashi, K., Uehara, H., Kandori, R., et al. 2005, *PASJ*, 57, 1
- Dunham, R. K., Rosolowsky, E., Evans, N. J., II, Cyganowski, C., & Urquhart, J. S. 2011, *ApJ*, 741, 110
- Elmegreen, B. G., & Scalo, J. 2004, *ARA&A*, 42, 211
- Falgarone, E., Levrier, F., & Hily-Blant, P. 2007, *EAS Publ. Ser.*, 23, 73
- Friesen, R. K., Di Francesco, J., Shirley, Y. L., & Myers, P. C. 2009, *ApJ*, 697, 1457
- Friesen, R. K., Medeiros, L., Schnee, S., et al. 2013, *MNRAS*, 436, 1513
- Fuller, G. A., & Myers, P. C. 1993, *ApJ*, 418, 273
- Glass, L., & Rice, S. A. 1968, *Phys. Rev.*, 176, 239
- Goodman, A. A., Barranco, J. A., Wilner, D. J., & Heyer, M. H. 1998, *ApJ*, 504, 223
- Gutermuth, R. A., Bourke, T. L., Allen, L. E., et al. 2008, *ApJ*, 673, L151
- Gwenlan, C., Ruffle, D. P., Viti, S., Hartquist, T. W., & Williams, D. A. 2000, *A&A*, 354, 1127
- Hennebelle, P., & Falgarone, E. 2012, *A&ARv*, 20, 55
- Ho, P. T. P., & Townes, C. H. 1983, *ARA&A*, 21, 239
- Humphreys, R. M., & Larsen, J. A. 1995, *AJ*, 110, 2183
- Juvela, M., Harju, J., Ysard, N., & Lunttila, T. 2012, *A&A*, 538, A133
- Kaplan, S. A., & Klimishin, I. A. 1964, *Soviet Astron.*, 8, 210
- Kawamura, A., Onishi, T., Mizuno, A., Ogawa, H., & Fukui, Y. 1999, *PASJ*, 51, 851
- Kawamura, A., Kun, M., Onishi, T., et al. 2001, *PASJ*, 53, 1097
- Kennicutt, R. C., Jr., & Evans, N. J., II 2012, *ARA&A*, 50, 531
- Kirk, H., Myers, P. C., Bourke, T. L., et al. 2013, *ApJ*, 766, 115
- Kitamura, Y., Sunada, K., Hayashi, M., & Hasegawa, T. 1993, *ApJ*, 413, 221
- Klein, B., Hochgürtel, S., Krämer, I., et al. 2012, *A&A*, 542, L3
- Klessen, R. S. 2011, *EAS Publ. Ser.*, 51, 133
- Kolmogorov, A. N. 1941, *Doklady Akademiia Nauk SSSR*, 30, 301
- Kritsuk, A. G., Norman, M. L., Padoan, P., & Wagner, R. 2007, *ApJ*, 665, 416
- Kritsuk, A. G., Nordlund, Å., Collins, D., et al. 2011, *ApJ*, 737, 13
- Kritsuk, A. G., Lee, C. T., & Norman, M. L. 2013, *MNRAS*, 436, 3247
- Kukulich, S. G. 1967, *Phys. Rev.*, 156, 83
- Kun, M., & Prusti, T. 1993, *A&A*, 272, 235
- Lad, K. N., & Pratap, A. 2004, *Phys. Rev. E*, 70, 051201
- Lagrois, D., & Joncas, G. 2011, *MNRAS*, 413, 721
- Landman, D. A., Roussel-Dupré, R., & Tanigawa, G. 1982, *ApJ*, 261, 732
- Larson, R. 1981, *MNRAS*, 194, 809
- Lebrun, F. 1986, *ApJ*, 306, 16
- Lemme, C., Wilson, T. L., Tiefertunk, A. R., & Henkel, C. 1996, *A&A*, 312, 585
- Lesieur, M. 1997, *Turbulence in Fluids* (Kluwer: Dordrecht)
- Levshakov, S. A., Henkel, C., Reimers, D., et al. 2013a, *A&A*, 553, A58 (Paper I)
- Levshakov, S. A., Reimers, D., Henkel, C., et al. 2013b, *A&A*, 559, A91
- Lynds, B. T. 1962, *ApJS*, 7, 1
- Maurly, A. 2011, *EAS Publ. Ser.*, 51, 169
- Maurly, A. J., André, P., Men'shchikov, A., Könyves, V., & Bontemps, S. 2011, *A&A* 535, A77
- McKee, C. F., & Ostriker, E. C. 2007, *ARA&A*, 45, 565
- Medina Tanco, G. A., Sabalisco, N., Jatenco-Pereira, V., & Opher, R. 1997, *ApJ*, 487, 163
- Menten, K. M., Walmsley, C. M., Krügel, E., & Ungerechts, H. 1984, *A&A*, 137, 108
- Miesch, M. S., & Bally, J. 1994, *ApJ*, 429, 645
- Miville-Deschênes, M.-A., Joncas, G., & Durand, D. 1995, *ApJ*, 454, 316
- Myers, P. C. 2014, *ApJ*, 781, 33
- Passot, T., Pouquet, A., & Woodward, P. R. 1988, *A&A*, 197, 228
- Phillips, J. P. 1999, *A&AS*, 134, 241
- Pineda, J. E., Goodman, A. A., Arce, H. G., et al. 2010, *ApJ*, 712, L116
- Press, W. H., Teukolsky, S. A., Vetterling, W. T., & Flannery, B. P. 1992, *Numerical Recipes in C* (Cambridge: Cambridge Uni. Press)
- Rydbeck, O. E. H., Sume, A., Hjalmarsen, et al. 1977, *ApJ*, 215, L35
- Sato, F., Mizuno, A., Nagahama, T., & Onishi, T. 1994, *ApJ*, 435, 279
- Scalo, J. M., 1984, *ApJ*, 277, 556
- Sreenivasan, K. R. 1991, *Ann. Rev. Fluid Mech.*, 23, 539
- Tafalla, M., Myers, P. C., Caselli, P., & Walmsley, C. M. 2004, *A&A*, 416, 191
- Tanaka, T., Nakamura, F., Awazu, Y., et al. 2013, *ApJ*, 778, 34
- Tóth, L. V., & Walmsley, C. M. 1996, *A&A*, 311, 981
- Ungerechts, H., Walmsley, C. M., & Winnewisser, G. 1980, *A&A*, 88, 259
- Wijeyesekera, S. D., & Kushick, J. N. 1979, *J. Chem. Phys.*, 71, 1397
- Williams, J. P., Lee, C. W., & Myers, P. C. 2006, *ApJ*, 636, 952
- Winnewisser, G., Churchwell, E., & Walmsley, C. M. 1979, *A&A*, 72, 215
- Yaglom, A. M. 1987, *Correlation Theory of Stationary and Related Random Functions I: Basic Results* (N.Y.: Springer-Verlag)
- Zuo, Y.-X., Yang, J., Shi, S. C., et al. 2004, *Chin. J. Astron. Astrophys.*, 4, 390

Appendix A: Ammonia spectra toward SS1, SS2, and L1251C and derived physical parameters

The ammonia spectra were analyzed in the same way as in Paper I. The radial velocity V_c ($\equiv V_{\text{LSR}}$), the linewidth Δv (FWHP), the optical depths τ_{11} and τ_{22} , the integrated ammonia emission $\int T_{\text{MB}} dv$, and the kinetic temperature T_{kin} , are well determined physical parameters, whereas the excitation temperature T_{ex} , the ammonia column density $N(\text{NH}_3)$, and the gas density n_{H_2} , which are less certain since they depend on the beam filling factor η , which is not known for unresolved cores (see Appendix A in Paper I).

The 1σ errors of the model parameters were estimated from the diagonal elements of the covariance matrix calculated for the minimum of χ^2 . The error in V_c was also estimated independently by the $\Delta\chi^2$ method (e.g., Press et al. 1992) to control both results. When the two estimates differed, the larger error was adopted. An independent control gives an analytical estimate of the uncertainty of the Gaussian line center by Landman et al. (1982):

$$\sigma_v \approx 0.69(\text{rms}/T_{\text{MB}}) \sqrt{\Delta_{\text{ch}} \cdot \Delta v}, \quad (\text{A.1})$$

where Δ_{ch} and Δv are the channel width and the linewidth, respectively, and the parameter rms is the root mean square noise level.

The results of our analysis are presented in Tables 1, A.1, and A.2. In Tables A.1 and A.2, Cols. 11 and 12 list the total optical depth τ_{tot} (see Eq. (A.4)) which is the maximum optical depth that an unsplit $(J, K) = (1, 1)$ or $(2, 2)$ rotational line would have at the central frequency if the hfs levels were populated with the same excitation temperature for the two lines $(1, 1)$ and $(2, 2)$. Column 13 lists the total column density $N_{\text{tot}}(\text{NH}_3)$ defined in Eq. (A.5).

For high signal-to-noise ratio (S/N) data (rms ~ 0.05 K per 0.039 km s^{-1} channel and $T_{\text{MB}} \sim 2$ K) and a narrow line ($\Delta v \sim 1 \text{ km s}^{-1}$), Eq. (A.1) gives $\sigma_v \sim 0.003 \text{ km s}^{-1}$, which is in line with the precision estimated from the covariance matrix. However, the accuracy of the line position centering is probably a few times lower taking into account irregular shifts ($\sim \frac{1}{4}\Delta_{\text{ch}}$) of the radial velocities V_c measured in our Effelsberg spectra (Levshakov et al. 2013b).

The errors of Δv depend on the S/N ratio and vary from $\sim 0.005 \text{ km s}^{-1}$ for strong ammonia lines ($S/N \gtrsim 30$) to $\sim 0.03 \text{ km s}^{-1}$ if $S/N \lesssim 10$. Since the uncertainty in the amplitude scale calibration was $\sim 20\%$ (Sect. 2), the same order of magnitude errors are obtained for T_{MB} , T_{rot} , T_{kin} , τ_{11} , and τ_{22} . For T_{ex} , $N_{\text{tot}}(\text{NH}_3)$, and n_{H_2} , we estimated lower bounds corresponding to the filling factor $\eta = 1$ (Paper I).

Examples of the NH₃(1, 1) and (2, 2) spectra observed toward SS1, SS2A, SS2B, SS2C, and L1251C are shown in Figs. A.1–A.5. The measured parameters at the positions with both detected inversion transitions $(1, 1)$ and $(2, 2)$ are listed in Tables A.1 and A.2.

The physical parameters, such as the total optical depth of an inversion line, τ_{tot} , the radial velocity, V_c , the linewidth, Δv , and the amplitude, \mathcal{A} , were estimated by fitting a Gaussian model, $T_{\text{syn}}(v)$, to the observed spectrum, $T_{\text{obs}}(v)$, by means of a χ^2 -minimization procedure:

$$\chi^2 = \sum [T_{\text{syn}}(v) - T_{\text{obs}}(v)]^2 / \text{rms}^2, \quad (\text{A.2})$$

where

$$T_{\text{syn}}(v) = \mathcal{A}\{1 - \exp[-\tau(v)]\}, \quad (\text{A.3})$$

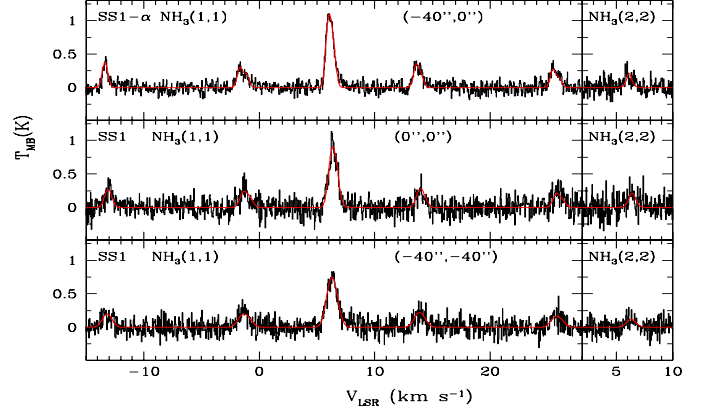


Fig. A.1. Ammonia NH₃(1, 1) and (2, 2) spectra toward the molecular core SS1. The channel spacing is 0.039 km s^{-1} ; the spectral resolution (full width at half peak, FWHP) is 0.045 km s^{-1} . The red curves show the fit of a one-component Gaussian model to the original data.

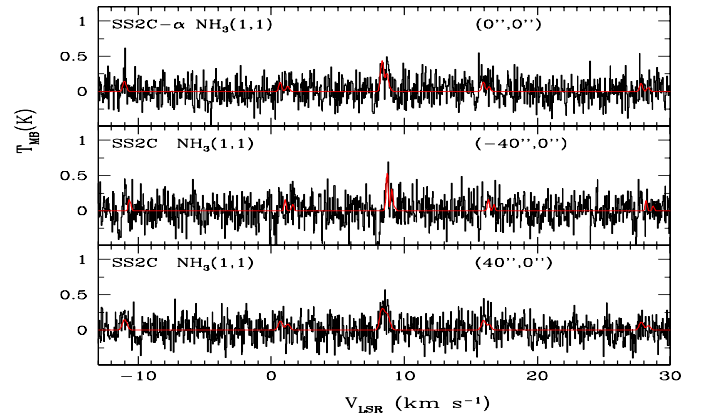


Fig. A.2. Inverse ammonia NH₃(1, 1) spectra (i.e., $-1 \times T_{\text{MB}}$, where T_{MB} is the originally measured main beam brightness temperature) toward the second serendipitously detected molecular core SS2C to show its signals, as obtained from off-positions, in emission. The “absorption” feature seen in the blue wing of the central NH₃ line at offsets $(0'', 0'')$, $(-40'', 0'')$, and $(40'', 0'')$ is the Doppler shifted ammonia emission line detected at offsets $(320'', 440'')$, $(280'', 440'')$, and $(360'', 440'')$ toward the source SS2B. The channel spacing is 0.039 km s^{-1} ; the spectral resolution FWHP is 0.045 km s^{-1} . The red curves show the fit of a one-component Gaussian model to the original data.

and the optical depth $\tau(v)$ at a given radial velocity v is

$$\tau(v) = \tau_{\text{tot}} \sum_{i=1}^n r_i \exp\left\{-2.773[(v - V_c) + v_i]^2 / (\Delta v)^2\right\}. \quad (\text{A.4})$$

Here, n is the number of magnetic hfs components of the inversion transition ($n = 18$ and 21 for the $(J, K) = (1, 1)$ and $(2, 2)$ inversion transitions), r_i is the relative intensity of the i th hfs line, and v_i is its velocity separation from the fiducial frequency (these parameters are taken from Kukolich 1967; and Rydbeck et al. 1977).

The total NH₃ column density is defined by

$$N(\text{NH}_3) = N_{11} \cdot [(1/3) \exp(23.2/T_{\text{rot}}) + 1 + (5/3) \exp(-41.5/T_{\text{rot}}) + (14/3) \exp(-105.2/T_{\text{rot}}) + \dots], \quad (\text{A.5})$$

where the relative population of all metastable levels of both ortho-NH₃ ($K = 3$), which is not observable, and para-NH₃

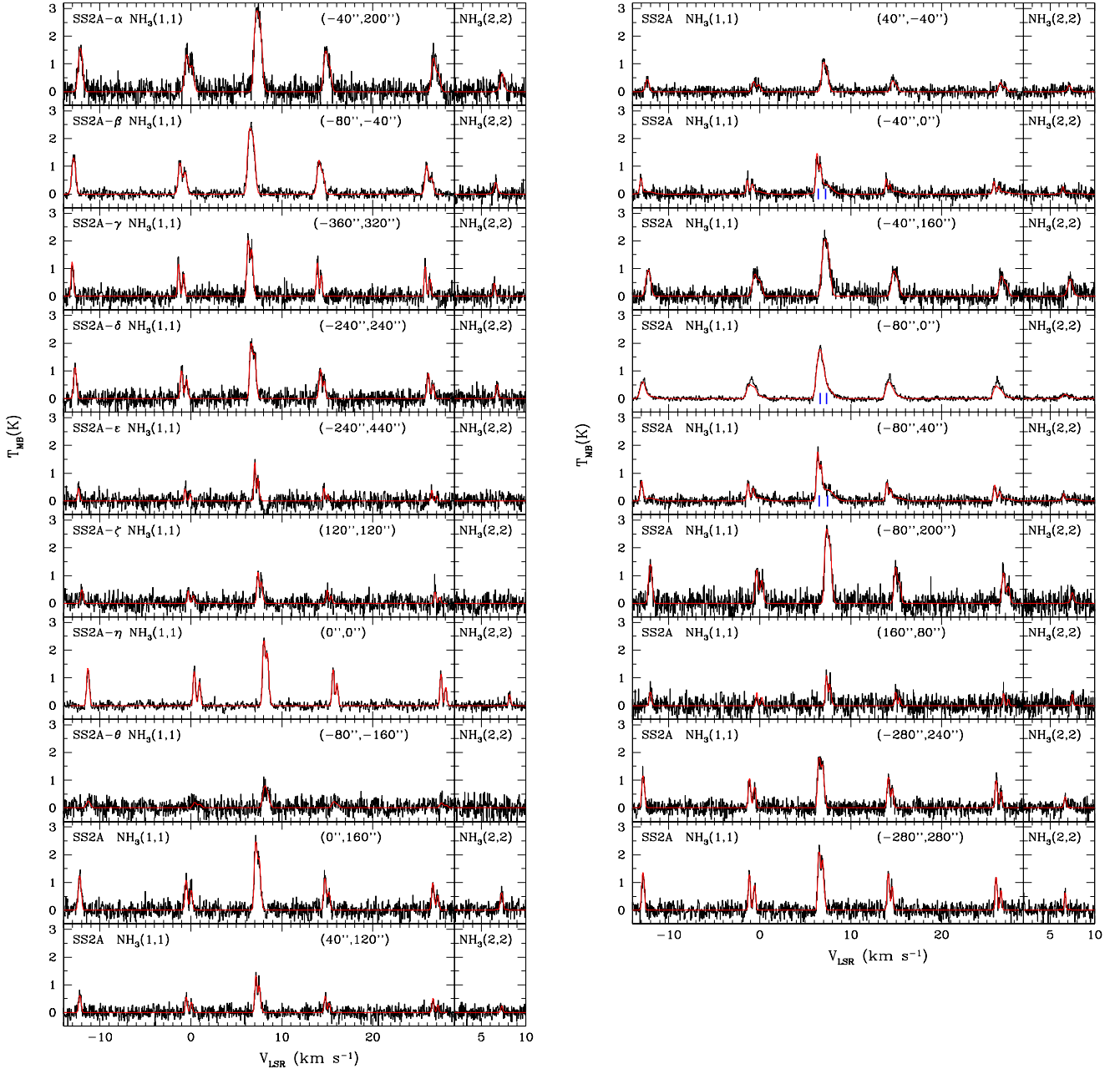


Fig. A.3. Ammonia $\text{NH}_3(1,1)$ and $(2,2)$ spectra toward the molecular core SS2A. The channel spacing is 0.039 km s^{-1} ; the spectral resolution $\text{FWHP} = 0.045 \text{ km s}^{-1}$. The red curves show the fit of a one- or two-component Gaussian model (the latter is marked by two vertical ticks at the position of the central NH_3 line) to the original data.

($K = 1, 2$) is assumed to be governed by the rotational temperature T_{rot} of the system at thermal equilibrium (Winnewisser et al. 1979).

If both inversion lines $\text{NH}_3(1,1)$ and $(2,2)$ are detected, we can estimate the kinetic temperature T_{kin} (Eq. (A.15) in Paper I) and find the thermal contribution to the observed linewidth, $v_{\text{obs}} = \Delta v / 2 \sqrt{\ln 2}$. The thermal velocity is defined by

$$v_{\text{th}} = \sqrt{\frac{2k_{\text{B}}T_{\text{kin}}}{m}}, \quad (\text{A.6})$$

where k_{B} is the Boltzmann constant, and m is the mass of a particle. For NH_3 , it is $v_{\text{th}} = 0.03 \sqrt{T_{\text{kin}}} \text{ (km s}^{-1}\text{)}$.

If the contribution of the thermal v_{th} and non-thermal (turbulent) v_{turb} components to the linewidth are independent of one another, then

$$v_{\text{obs}} = \sqrt{v_{\text{th}}^2 + v_{\text{turb}}^2}, \quad (\text{A.7})$$

and the non-thermal velocity dispersion σ_{turb} along the line of sight is $\sigma_{\text{turb}} = v_{\text{turb}} / \sqrt{2}$. This value can be compared with the thermal sound speed

$$c_{\text{s}} = (\tilde{\gamma}P_{\text{th}}/\rho)^{1/2}, \quad (\text{A.8})$$

where P_{th} is the thermal pressure and ρ the gas density. For an isothermal gas ($\tilde{\gamma} = 1$), $c_{\text{s}} = 0.06 \sqrt{T_{\text{kin}}} \text{ (km s}^{-1}\text{)}$.

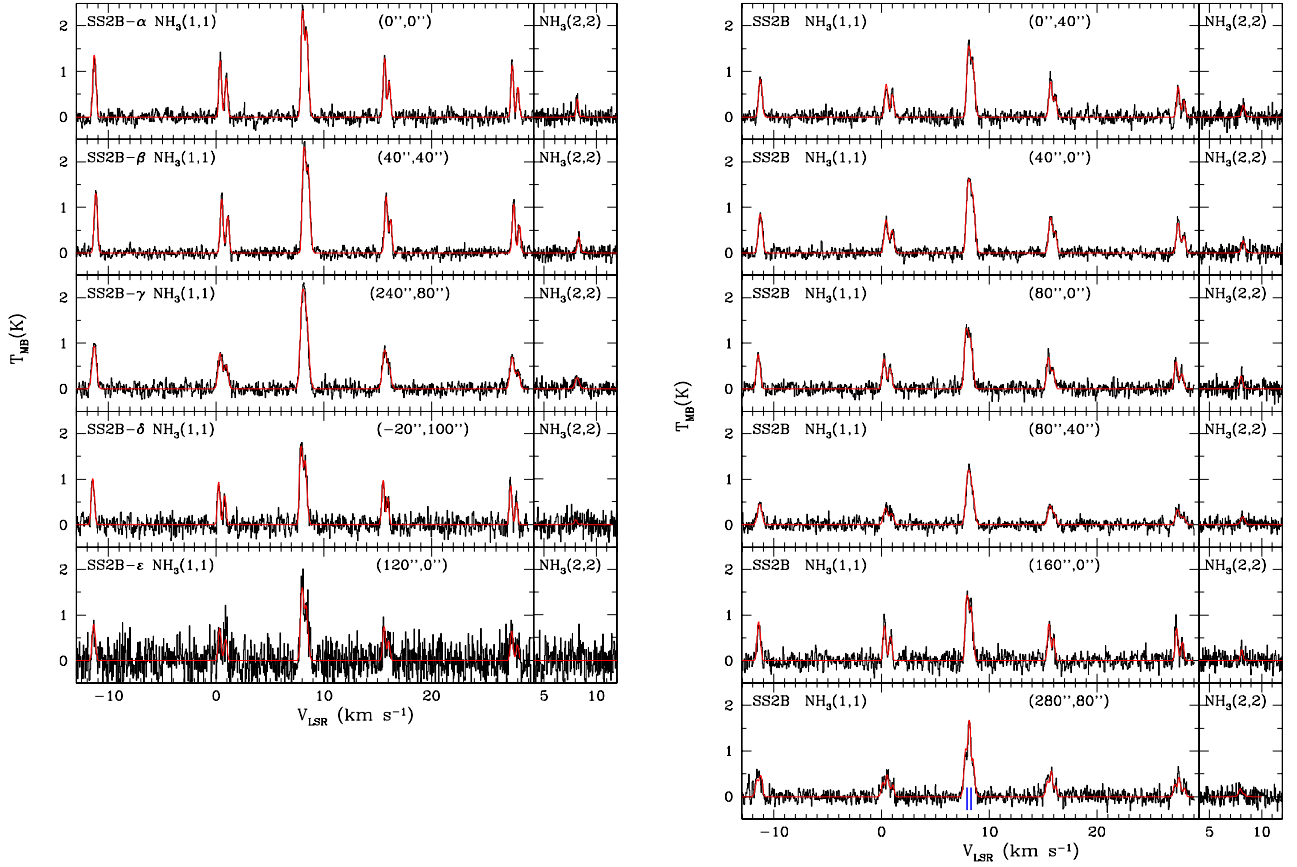


Fig. A.4. Same as Fig. A.3 but for the serendipitously detected starless molecular core SS2B.

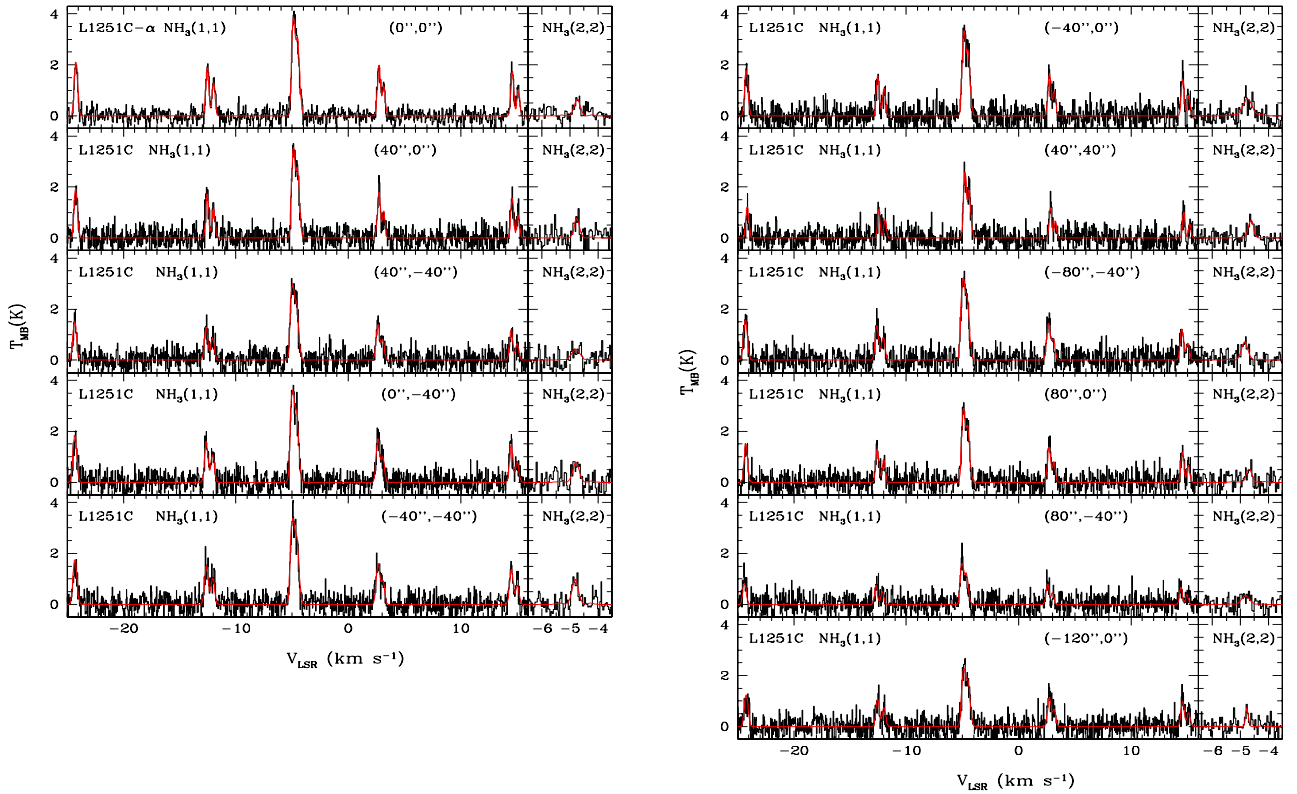


Fig. A.5. Ammonia NH₃(1, 1) and (2, 2) spectra toward the source L1251C. The channel spacing is 0.039 km s⁻¹; the spectral resolution *FWHP* = 0.045 km s⁻¹. The red curves show the fit of a one-component Gaussian model to the original data. The model parameters are listed in Table A.2.

Table A.1. Observed parameters of the NH₃(1, 1) and (2, 2) lines and calculated model parameters for SS1 and SS2.

Peak Id.	$\Delta\alpha$ (")	$\Delta\delta$ (")	V_{LSR} (km s ⁻¹)	Δv (km s ⁻¹)	T_{MB} (K)	T_{ex} (K)	T_{rot} (K)	T_{kin} (K)	$n_{\text{H}_2}/10^4$ (cm ⁻³)	τ_{11}	τ_{22}	$N_{\text{tot}}/10^{14}$ (cm ⁻²)
SS1												
α	-40	0	6.14	0.54	1.1	5.5	12.5	13.6	1.8	1.4	0.1	1.8
	0	0	6.41	0.69	0.9	5.8	13.6	15.1	1.9	0.9	0.09	1.4
	-40	-40	6.32	0.95	0.8	6.9	12.9	14.1	3.4	0.5	0.04	1.3
SS2A												
α	-40	200	7.36	0.47	2.9	6.1	11.0	11.8	2.7	6.0	0.3	9.1
β	-80	-40	6.62	0.42	2.4	5.5	10.0	10.5	2.2	6.4	0.2	9.0
γ	-360	320	6.46	0.24	2.0	4.9	10.2	10.8	1.6	9.1	0.4	6.3
δ	-240	240	6.78	0.30	1.9	5.0	10.8	11.5	1.6	7.0	0.3	5.7
	0	160	7.29	0.30	2.5	6.0	11.5	12.4	2.4	4.9	0.3	4.4
	40	120	7.31	0.24	1.3	4.6	10.4	11.0	1.3	4.3	0.2	2.8
	40	-40	7.15	0.43	1.1	4.5	11.8	12.7	1.1	2.7	0.2	2.5
	-40	0 ^a	6.44	0.26	1.5	4.0	11.5	12.3	0.7	1.5	0.09	0.8
			7.25	1.37						0.4		
	-40	160	7.26	0.54	2.1	5.3	12.9	14.2	1.6	4.2	0.4	5.3
	-80	0 ^a	6.64	0.59	1.8	3.5	9.8	10.3	4.6	1.8	0.06	2.4
			7.36	1.26						0.5		
	-80	40 ^a	6.52	0.28	1.8	3.9	10.7	11.4	0.7	2.0	0.09	1.2
			7.44	1.43						0.5		
	-80	200	7.48	0.37	2.7	6.0	9.8	10.3	3.1	5.5	0.2	7.7
	160	80	7.49	0.22	1.1	4.3	13.3	14.7	0.8	4.4	0.4	1.7
	-280	240	6.69	0.28	1.8	4.7	9.8	10.3	1.4	9.6	0.3	7.9
	-280	280	6.68	0.24	2.1	5.0	9.6	10.1	1.7	10.4	0.3	8.1
SS2B												
α	0	0	8.19	0.26	2.3	5.4	9.7	10.2	2.2	7.7	0.2	6.9
β	40	40	8.32	0.29	2.3	5.4	9.6	10.0	2.3	6.8	0.2	7.1
γ	240	80	8.18	0.43	2.2	6.3	9.9	10.4	3.5	2.9	0.1	4.9
	0	40	8.24	0.32	1.6	4.7	10.2	10.8	1.3	5.7	0.2	5.0
	40	0	8.23	0.37	1.6	4.7	10.3	10.9	1.4	5.5	0.2	5.5
	80	0	8.04	0.34	1.3	4.3	10.3	10.8	1.0	6.7	0.3	5.8
	80	40	8.18	0.44	1.2	5.5	11.1	11.9	2.0	1.7	0.09	2.1
	160	0	8.09	0.27	1.4	4.3	9.4	9.8	1.1	8.0	0.2	6.6
	280	80 ^a	8.30	0.25	1.7	3.8	8.5	8.8	0.7	1.2	0.02	1.0
			7.95	0.33						1.8		

Notes. ^(a) Asymmetric profile; parameters of the second component are given in the second row.

Table A.2. Observed parameters of the NH₃(1, 1) and (2, 2) lines and calculated model parameters for L1251C.

Peak Id.	$\Delta\alpha$ (")	$\Delta\delta$ (")	V_{LSR} (km s ⁻¹)	Δv (km s ⁻¹)	T_{MB} (K)	T_{ex} (K)	T_{rot} (K)	T_{kin} (K)	$n_{\text{H}_2}/10^4$ (cm ⁻³)	τ_{11}	τ_{22}	$N_{\text{tot}}/10^{15}$ (cm ⁻²)
α	0	0	-4.722(3)	0.290	3.9	7.3	10.0	10.5	5.9	6.4	0.2	0.8
	40	0	-4.733(5)	0.28	3.5	7.0	10.5	11.1	4.4	6.2	0.3	0.7
	40	-40	-4.826(7)	0.33	3.0	6.6	9.8	10.3	4.2	5.0	0.2	0.7
	0	-40	-4.818(5)	0.33	3.6	7.3	10.9	11.7	4.7	5.2	0.3	0.7
	-40	-40	-4.805(6)	0.35	3.4	6.9	11.9	12.9	3.5	5.4	0.4	0.6
	-40	0	-4.718(6)	0.29	3.3	6.8	10.5	11.1	4.1	5.9	0.3	0.7
	40	40	-4.625(6)	0.24	2.6	6.3	11.4	12.2	2.8	4.7	0.3	0.4
	-80	-40	-4.797(7)	0.34	3.2	7.0	11.4	12.2	3.9	4.5	0.3	0.6
	80	0	-4.755(6)	0.29	2.9	6.4	10.4	11.0	3.4	5.4	0.2	0.6
	80	-40	-4.88(1)	0.29	1.6	4.7	10.9	11.7	1.3	5.6	0.3	0.4
	-120	0	-4.728(9)	0.33	2.3	5.4	12.0	12.9	1.8	6.2	0.4	0.5

The Mach number is defined locally as

$$\mathcal{M}_s = \sigma_{\text{turb}}/c_s. \quad (\text{A.9})$$

The relative errors $\delta_{\Delta v}$ in Δv and δ_{τ} in T_{kin} propagate into the relative error of the Mach number, $\delta_{\mathcal{M}}$, as

$$\delta_{\mathcal{M}} = \sqrt{\left(\frac{\delta_{\Delta v}}{8 \ln 2} \frac{\Delta v^2}{\sigma_{\text{turb}}^2}\right)^2 + \left(\frac{\delta_{\tau}}{4} \frac{v_{\text{th}}^2}{\sigma_{\text{turb}}^2}\right)^2 + \left(\frac{\delta_{\tau}}{2}\right)^2}, \quad (\text{A.10})$$

where $\delta_{\tau} \sim 0.2$ and $\delta_{\Delta v} \sim 0.01\text{--}0.05$ (see Table 1).

The value of the linewidth Δv and the core radius R can be used to estimate the virial mass (e.g., Lemme et al. 1996):

$$M_{\text{vir}} = 250\Delta v^2 R, \quad (\text{A.11})$$

where Δv is in km s⁻¹, R in pc, and M_{vir} in solar masses M_{\odot} .